



Eidgenössische Technische Hochschule Zürich  
Swiss Federal Institute of Technology Zurich

BACHELOR THESIS

# Automatic Single Qubit Routines

*Author:*

Livio Ciorciaro

*Supervisor:*

Johannes Heinsoo

Spring 2015

Laboratory for Solid State Physics  
Quantum Device Lab



# Abstract

Superconducting qubits are promising candidates for building scalable quantum computers. A software suite has been developed in the Quantum Device Lab for the automatic calibration of qubits and their control pulses. This software is now also used for other types of experiments and we have implemented a new framework which makes it easily extendable for future developers. This thesis gives an introduction to the theoretical background of superconducting qubits, outlines the structure of the software suite, and discusses the automatic routines we have implemented in the new framework. These include standard calibration experiments (Rabi, Ramsey, QScale, CalTom), measurements of the coherence time ( $T_1$ ,  $T_2^*$ ,  $T_2$ ) and gate fidelity (randomized benchmarking), and experiments on the  $ef$ -transition.



# Contents

<b>1</b>	<b>Introduction</b>	<b>1</b>
<b>2</b>	<b>Quantum Information Experiments with cQED</b>	<b>3</b>
2.1	The Transmon Qubit . . . . .	3
2.2	Qubit Control and State Readout . . . . .	5
2.3	Control Pulse Generation . . . . .	7
<b>3</b>	<b>Experiment Control Software</b>	<b>9</b>
3.1	Overview . . . . .	9
3.2	New Structure of the Pattern Generation and Analysis . . . . .	11
3.3	Adding New Experiment Types . . . . .	12
3.4	Outlook . . . . .	13
<b>4</b>	<b>Automatic Single Qubit Routines</b>	<b>15</b>
4.1	Pulse Model . . . . .	15
4.2	Calibration Experiments . . . . .	16
4.3	Coherence Time . . . . .	19
4.4	Randomized Benchmarking . . . . .	21
4.5	<i>ef</i> -transition Experiments . . . . .	24
<b>5</b>	<b>Summary</b>	<b>29</b>
	<b>Summary</b>	<b>29</b>
	<b>Acknowledgements</b>	<b>31</b>
	<b>References</b>	<b>33</b>
<b>A</b>	<b>Input and Output of Automatic Routines</b>	<b>41</b>
A.1	Input and Output Parameters . . . . .	41
A.2	Example Graphical Output of QubitCalib . . . . .	43



# 1 Introduction

The ability of computers to store and process huge amounts of information has become essential for many applications. The possibilities of classical information processing however are limited, as there are problems for which the number of steps a classical computer needs to find the solution grows exponentially with the size of the input. Prime factorization is one such problem and the exponential complexity makes it so hard to solve that it is used in most common encryption algorithms. [Nielsen 00]

The idea of quantum computing was first published in the 1980s [Feynman 82, Wiesner 83, Deutsch 85]. The basic unit of information in a quantum computer is called quantum bit or qubit. It is a two-level quantum system with the states  $|0\rangle$  and  $|1\rangle$  which correspond to the classical logical states. The difference between a classical bit and a qubit is that the qubit can also exist in superposition states  $c_0|0\rangle + c_1|1\rangle$ ,  $|c_0|^2 + |c_1|^2 = 1$ . This extends the computational possibilities, for example it allows an operation in a quantum computer to act on multiple input states simultaneously.

Several algorithms for quantum computers have been presented which outperform their fastest possible classical counterparts [Deutsch 92, Grover 96, Shor 97]. The most popular example is Shor's algorithm for prime factorization which has only polynomial complexity and is exponentially faster than any classical algorithm. This algorithm has been implemented for small numbers in different quantum computer systems [Vandersypen 01, Gilowski 08, Politi 09].

Another important application for quantum computers is the simulation of other quantum mechanical systems, as originally proposed by Feynman and Deutsch [Feynman 82, Deutsch 85]. Because the quantum computer behaves quantum mechanically itself it can be used to imitate another quantum mechanical system, while also allowing to engineer the interactions in that system [Blatt 12, Georgescu 14]. For example interactions in one-dimensional quantum spin chains have been simulated [Friedenauer 08, Kim 10, Lanyon 11, Salathé 15].

There are different physical realizations of quantum computers. Some of the two-level systems that have been used to implement qubits are nuclear or electron spin states in a magnetic field (NMR) [Cory 97, Gershenfeld 97], electronic states of trapped atoms or ions [Cirac 95], polarization states of photons [Knill 01], electron spins in field induced quantum dots [Loss 98] or nitrogen-vacancy centers in diamond [Neumann 10], and superconducting circuits [Zagoskin 07]. All of these have turned out to be challenging because the qubit must be shielded from its environment in order to have a sufficiently long coherence time. Yet coupling must be available to be able to read out and control the qubit state precisely.

In our setup a type of superconducting qubit called the transmon qubit [Koch 07] is used, which will be explained in Section 2. Qubits based on superconducting circuits referred to as circuit quantum electrodynamics (cQED) have several advantages over other implementations. Most important is the fact that many of the physical properties of the system can be engineered, unlike in other systems, where they are given by nature. Moreover, standard lithography techniques can be used to fabricate the on-chip circuits, which is advantageous when it comes to scalability. And with transition frequencies on the scale of a few gigahertz, i. e. microwave frequencies, the necessary electronic equipment for the control and readout of the qubits is already available.

The state of a transmon qubit is controlled by applying short resonant microwave pulses. To achieve control with high precision these pulses have to be carefully tuned to the qubit. The amplitude, frequency, and shape of a pulse determine its effect on the qubit state. Therefore it is necessary to calibrate these parameters before experiments can be run on a qubit. The calibration needs to be repeated regularly as the properties of the qubit vary slightly due to coupling to the environment and drifts of the devices. For this, an automated calibration routine was developed in our lab for single qubit gates [Menke 13, Landig 13] and for multi-qubit gates [Heinsoo 13].

This thesis gives a short overview of the basic considerations involved in controlling and measuring a single superconducting qubit state and how they are implemented in the Quantum Device Lab. For future developers in our lab this thesis should serve as a documentation of the framework and the experiments that are already implemented.



## 2 Quantum Information Experiments with cQED

Building a quantum computer requires a scalable physical implementation of two-level systems that can be used as qubits, coherent control and readout of these qubits and sufficiently long coherence times for the last two [DiVincenzo 00]. In the case of cQED, the qubit is a superconducting circuit and is controlled with resonant microwave pulses and a DC line to control the magnetic flux. In this Chapter, I describe how this is realized in the Quantum Device Lab and summarize the theoretical background. I start with the qubit itself and then explain how coupling to a cavity is used to drive qubit transitions and measure its state. Finally, I describe the process of generating arbitrary microwave pulses to control the qubit state.

### 2.1 The Transmon Qubit

The qubit implementation chosen in our lab is a type of superconducting qubit called transmon qubit [Koch 07]. It is a type of charge qubit [Büttiker 87] which is represented in the general case by the circuit diagram shown in Fig. 1. The core part is a SQUID (Superconducting QUantum Interference Device) loop, a superconducting loop interrupted by two Josephson junctions [Josephson 62] with Josephson energies  $E_{J,1}$  and  $E_{J,2}$ . If the two Josephson energies are equal, the SQUID loop corresponds to a single Josephson junction with energy  $E_J(\Phi) = 2E_{J,1} |\cos(\pi\Phi/\Phi_0)|$  and capacitance  $C_J$ . The Josephson energy depends on the magnetic flux  $\Phi$  through the loop, which makes it tunable by applying a local magnetic field. Cooper pairs can tunnel from the reservoir, which is connected to the ground, through the Josephson junctions to the island. The island is capacitively coupled to a voltage source  $V_g$  through a gate capacitance  $C_g$ . In a transmon qubit the SQUID loop is shunted by a large capacitance  $C_S$  such that the total Josephson energy  $E_J$  is much greater than the total charging energy  $E_C = \frac{1}{2}e^2 / (C_J + C_S)$  of the SQUID loop. This regime where  $E_J \gg E_C$  is called the transmon regime and makes the energy levels of the qubit independent of the charge on the island and thus much less sensitive to charge noise [Koch 07].

The charge qubit is described by the Hamiltonian [Büttiker 87, Baur 12]

$$\hat{H} = 4E_C (\hat{N} - n_g)^2 - E_J(\Phi) \cos \hat{\delta} \quad (1)$$

where  $\hat{N}$  is the number operator for the excess Cooper pairs on the island compared to the neutral state,  $n_g = -C_g V_g / 2e$  is the gate charge on the capacitance  $C_g$  in units of  $2e$ , and  $\hat{\delta}$  is the phase difference across the Josephson junction. The Schrödinger equation can be analytically solved in the phase representation with eigenstates  $\hat{\delta} |\delta\rangle = \delta |\delta\rangle$  and  $\hat{N} = -i \frac{\partial}{\partial \delta}$  [Cottet 02].

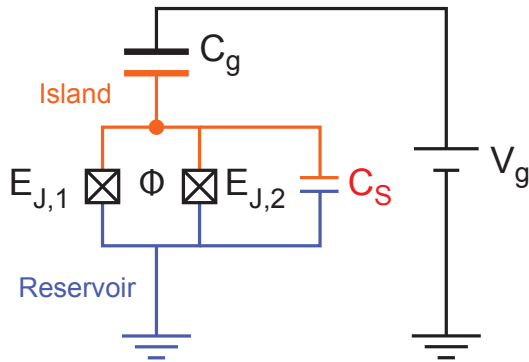


**Figure 1:** Circuit diagram of a charge qubit. It consists of a SQUID loop with Josephson energies  $E_{J,1}$  and  $E_{J,2}$  shunted by a capacitance  $C_S$  and is capacitively coupled to a voltage source  $V_g$  through a capacitance  $C_g$ . Figure adapted from [Baur 12].

The energy levels of a Cooper pair box in different regimes are shown in Fig. 2. The levels flatten with increasing  $E_J/E_C$  and are practically independent of the gate charge  $n_g$  in the transmon regime, as seen in Fig. 2(c). A more thorough discussion of the different regimes and the derivation and solution of the charge qubit Hamiltonian can be found in M. Baur's PhD thesis [Baur 12].

For quantum information experiments we usually restrict ourselves to the lowest two energy levels. The eigenstates of these levels are denoted as  $|g\rangle$  and  $|e\rangle$  for *ground* and *excited*. The eigenstate of the third energy level is called  $|f\rangle$ . In the subspace of the first two energy levels, the single qubit Hamiltonian can be written as

$$\hat{H}_{ge} = \frac{1}{2} \hbar \omega_{ge} \hat{\sigma}_z, \quad (2)$$

with the Pauli z-matrix  $\hat{\sigma}_z$ . This is an effective spin-1/2 Hamiltonian with the transition frequency  $\omega_{ge} = \frac{1}{\hbar} (E_e - E_g)$ , a two-level system that can be used as qubit. When the third energy level is considered, the transition between  $|e\rangle$  and  $|f\rangle$  is treated analogously with a transition frequency  $\omega_{ef} = \frac{1}{\hbar} (E_f - E_e)$ . To be able to drive transitions between the first two energy levels without affecting other transitions, the spectrum has to be anharmonic. In the case of the transmon qubit, the energy difference between neighbouring energy levels decreases in higher levels. Since only the first three energy levels are relevant, the anharmonicity is defined as  $\alpha = \omega_{ef} - \omega_{ge}$ , the difference between the first two transition frequencies.

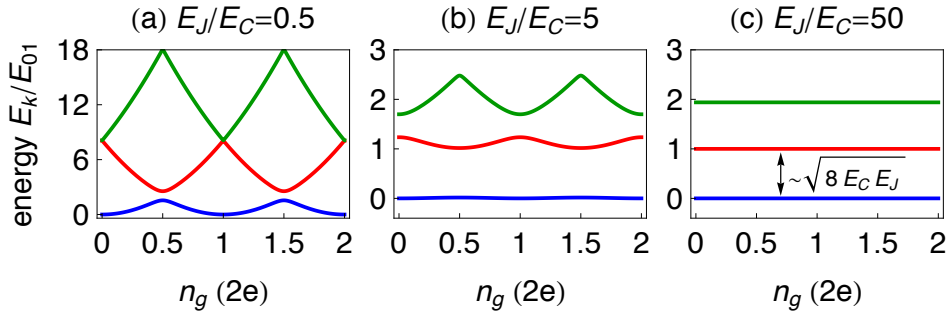


**Figure 2:** Energy levels of a Cooper pair box in different regimes. The energy levels flatten with increasing  $E_J/E_C$  and are practically independent of the gate charge  $n_g$  in the transmon regime, shown in (c). The energy unit  $E_{01}$  is the energy difference between the first two levels at  $n_g = 0.5$ . Figure from [Baur 12].

## 2.2 Qubit Control and State Readout

The transmon qubit described in the previous Section provides the two-level system which is used to store quantum information. What is needed next is the possibility to manipulate and read out the qubit state. To achieve this, the qubit is capacitively coupled to a coplanar waveguide resonator with resonance frequency  $\omega_r$ , which is analogous to an optical cavity used in quantum optics [Blais 04, Wallraff 04]. The interaction of a two-level system inside a cavity is described by the Jaynes-Cummings Hamiltonian [Jaynes 63]

$$\hat{H}_{\text{JC}} = \frac{1}{2}\hbar\omega_{ge}\hat{\sigma}_z + \hbar\omega_r\hat{a}^\dagger\hat{a} + \hbar g \left( |g\rangle\langle e| \hat{a}^\dagger + |e\rangle\langle g| \hat{a} \right), \quad (3)$$

where  $\hat{a}^\dagger$  and  $\hat{a}$  are the creation and annihilation operators for the cavity mode, respectively, and  $g$  is the coupling strength between the cavity and the qubit. The first and second terms of the Hamiltonian are the energies of the isolated qubit and photon the modes in the cavity. The third term is the interaction term which allows photons to be absorbed or emitted by the qubit, thereby raising or lowering the qubit state. Because of the small anharmonicity of the transmon qubit, its higher energy states also have to be taken into account for an exact treatment [Koch 07]. However, this does not change the results qualitatively.

The qubit is operated in the dispersive regime, where the detuning of the qubit and resonator frequencies is large compared to the coupling, i. e.  $|\omega_{ge} - \omega_r| \gg g$ . The Hamiltonian then takes the form

$$\hat{H}_{\text{disp}} = \frac{1}{2}\hbar\omega'_{ge}\hat{\sigma}_z + \hbar(\omega_r + \chi\hat{\sigma}_z)\hat{a}^\dagger\hat{a} \quad (4)$$

with a qubit frequency  $\omega'_{ge}$  renormalized by the Lamb shift [Koch 07, Baur 12]. The dispersive shift  $\chi$  depends on the coupling strength and the detuning of the qubit from the resonator. The interpretation of this Hamiltonian is that depending on the state of the qubit, the resonator frequency is shifted by  $\pm\chi$ . This can be seen in the transmission spectrum of the resonator and is used to measure the qubit state [Blais 04].

The qubit state readout is done by applying a weak microwave drive

$$\hat{H}_d = \hbar\varepsilon_d (\hat{a}^\dagger e^{-i\omega_d t} + \hat{a} e^{i\omega_d t}) \quad (5)$$

with amplitude  $\varepsilon_d$  and frequency  $\omega_d = \omega_r - \chi$  to the resonator. The in-phase and quadrature components  $I(t) = \langle \hat{a}^\dagger + \hat{a} \rangle$  and  $Q(t) = \langle i(\hat{a}^\dagger - \hat{a}) \rangle$  (see Section 2.3) of the transmitted signal  $S(t) = I(t) + iQ(t)$  are measured [Lang 14]. The measured  $Q(t)$  transmission with the qubit in the ground and excited state is shown in Fig. 3. The excited state response decays to the ground state response as the qubit decays to its ground state during the measurement. The phase of the signal is selected such that the I component vanishes and the Q component has all the information about the qubit state, maximizing the signal-to-noise ratio for the Q component. The  $|e\rangle$  state population  $p_e$  of an unknown output state  $|m\rangle = (1 - p_e)|g\rangle + p_e|e\rangle$  is proportional to the integrated difference  $\int Q_e(t) - Q_m(t) dt$  of the measured transmission for the qubit in the  $|m\rangle$  and  $|e\rangle$  states [Bianchetti 09]. To get values between 0 and 1 for the population it is scaled to the difference between the excited and ground state response and given by

$$p_e = \frac{\int Q_e(t) - Q_m(t) dt}{\int Q_e(t) - Q_g(t) dt}. \quad (6)$$

This method can be generalized for measurements including the  $|f\rangle$  state [Bianchetti 10] and multiple qubits [Filipp 09]. In these cases the scaling must be chosen accordingly.

Coherent control of the qubit state is possible by applying a strong microwave drive resonant to the qubit transition frequency. This can be done either through the resonator or through an additional charge line capacitively coupled to the qubit. The microwave drive is described by the Hamiltonian in Eq. (5) with amplitude  $\varepsilon_d$  and frequency  $\omega_d$ . In a frame rotating at the drive frequency  $\omega_d$  this produces the Hamiltonian

$$\hat{H} = \frac{\Omega_R}{2} \hat{\sigma}_x, \quad (7)$$

where  $\Omega_R = 2\varepsilon_d g / (\omega_r - \omega_d)$  is the Rabi frequency [Blais 07]. In the Bloch sphere picture this Hamiltonian generates rotations around the x-axis. The angle by which the state is rotated

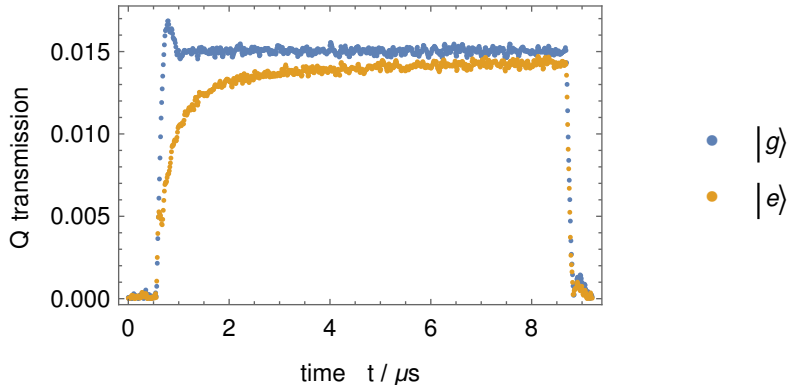


**Figure 3:** One quadrature of the measured resonator transmission for the qubit in the ground and excited state. The excited state response decays to the ground state response.

depends on the product of the Rabi frequency and the time during which the drive is applied and can therefore be set by choosing the correct pulse duration and amplitude. The phase of the microwave pulse determines the axis of the rotation. With these tools, arbitrary rotations around any axis on the equatorial plane in the Bloch sphere can be performed. This is sufficient to implement any single qubit gate. The rotations are usually chosen around the x- or y-axis and are labeled by the rotation axis and angle, e. g.  $X(\pi)$  or  $Y(\frac{\pi}{2})$ .

Another qubit parameter which can be controlled is its transition frequency. As described in Section 2.1 it depends on the magnetic flux through the SQUID loop. It is tuned by applying a direct current to a flux line running close to the SQUID loop, which creates a local magnetic field. The magnetic field must be well localized in order to avoid influencing other qubits on the same chip. Detuning the qubit with respect to the microwave drive can be used to implement rotations around the z-axis for a single qubit, as the qubit is taken out of its rotating reference frame while it is detuned. More commonly qubit frequency tuning is used for multi-qubit operations, where coupling between two qubits is controlled by tuning them on- and off-resonance [Majer 07].

### 2.3 Control Pulse Generation

To achieve the precise control over the phase and amplitude of the pulses needed for accurate control of the qubit state the signal is modulated with an IQ-mixer. The IQ-mixer has three input ports (LO, I, Q) and one output port. At the LO port a continuous wave with frequency  $\omega_{\text{LO}}$  is applied, which is split into two components in the mixer. One component remains in-phase with the input signal and is effectively multiplied by the voltage on the I port using

a non-linear element. The other component is phase-shifted by  $-\pi/2$  and multiplied by the voltage on the Q port. The two components are then added together. For DC voltages on the I and Q ports this results in an output signal [Baur 12]

$$s_{\text{RF}}(t) = I \cos(\omega_{\text{LO}}t) + Q \sin(\omega_{\text{LO}}t) = A \cos(\omega_{\text{LO}}t + \phi). \quad (8)$$

The amplitude and phase of the output are given by  $A = \sqrt{I^2 + Q^2}$  and  $\phi = \arctan(Q/I)$ . If time dependent voltages  $I(t) = I \cos(\omega_{\text{IF}}t + \phi)$  and  $Q(t) = Q \cos(\omega_{\text{IF}}t + \phi + \phi_Q)$  with an intermediate frequency  $\omega_{\text{IF}}$  are applied instead, the output consists of two sideband signals at frequencies  $\omega_{\text{LO}} \pm \omega_{\text{IF}}$ . One of the sidebands can be eliminated by choosing  $I = Q$  and  $\phi_Q = \pm\pi/2$ . The amplitude of the output signal is then controlled by the amplitude  $I = Q$  and the phase can be adjusted with the phase  $\phi$  of the input signal [Baur 12].

With IQ-modulation simultaneous control of the phase and amplitude of the signal is achieved and it allows us to filter out DC noise from the arbitrary waveform generators (AWGs) with single-sideband mixing. The upconversion is used to get from an intermediate frequency of around 150 MHz, which is well inside the bandwidth of our AWGs, to the high qubit frequency usually in the range of 4–10 GHz. Analogously the measured signal is downconverted to an intermediate frequency due to the limited detection bandwidth.

With these tools pulses for arbitrary single qubit gates can be generated. The software that generates the pulses for an experiment uses parameters from the calibration to write the waveforms that the AWGs should output. In the next Chapters I will discuss some of these calibration operations.

## 3 Experiment Control Software

The experiment control software started as a small set of scripts for generating modulation pulses and analyzing the measured signals, and has since grown into a large software suite. In this Chapter, I outline the structure of the software components and data flow. I give a motivation for a software design improvement, explain the new framework we implemented, and show how to make use of it.

### 3.1 Overview

The software that controls experiments on the qubits consists of three components. QubitCalib is the main component that a user interacts with. It has a visual interface which is used to start measurements and show results from the analysis. CleanSweep is the interface to the hardware. It sends the pulse sequences to the arbitrary waveform generators and collects the data from the FPGA used for the measurement. The third component are scripts in the Wolfram Mathematica language that generate the pulse patterns for the experiments and analyze the data.

Figure 4 shows the data flow in an experiment and how the three components work together. When an experiment is started, QubitCalib writes a file `QubitCalib.ini` with the experiment type and all relevant file paths, and calls the appropriate Mathematica script for the experiment. The script loads the specified `QubitCalib.ini` and `pattern.config.cfg` files. The `pattern.config.cfg` file, often referred to as pattern config, contains all physical parameters needed for the pattern generation, like qubit frequencies and pulse amplitudes. With these parameters the pulse sequences are generated and written to files accessible to the AWGs. The parameters from the pattern config file and any additional, experiment-specific parameters that were used are written to a file `Pulses.txt` for later analysis and backing up. When the Mathematica script finishes, QubitCalib tells CleanSweep to run the experiment with the generated pulses. The data is saved and the `Pulses.txt` file is backed up as `Pulses.dat`. Once the measurement is finished, QubitCalib runs the Mathematica script for the analysis. The analysis script loads the `pulses.dat` file to get the physical parameters which were used in the pulse generation and reads in the data.

Before QubitCalib was introduced each type of measurement had two dedicated scripts for the pattern generation and analysis which were run by hand. When this task was automated with QubitCalib, the same scripts were still used; two separate files for every experiment type. However, a lot of code was identical in all files as it was doing non-specific tasks like loading measurement parameters or reading data.

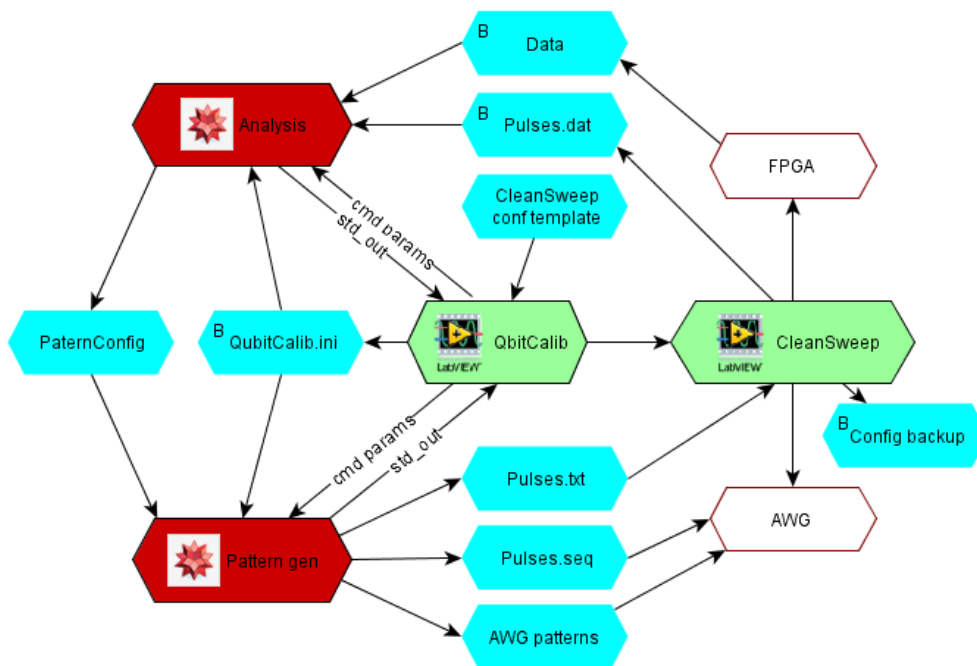


**Figure 4:** Data flow between the three components of the experiment control software. Green boxes are LabView programs, red boxes are Mathematica scripts, blue boxes are files and white boxes are hardware components. QubitCalib is the central unit which calls Mathematica scripts or CleanSweep when necessary. Several files are used for communication between the components. Files marked with an uppercase B are backed up. Figure from [Heinsoo 13].



In an effort to improve the organization of the code which is constantly growing with the addition of new experiments, we implemented a new framework for the Mathematica component of the software suite. The main objectives for the new framework were:

- **Reusability:** The code should be written in a general way, allowing other developers to reuse functions and features which are not specific to the original application.
- **Extendability:** Adding new experiments and features should be simple and not require extensive knowledge about the whole framework. This means that the framework must be designed from the start in a way that allows extension.
- **Uniformity:** The measurements should follow similar steps and use similar naming conventions for the parameters they use and output. This way it is easier to understand already implemented experiments and there is a reference when implementing new ones.

These goals have many aspects in common, for example extendable code has to be reusable for the most part aswell. Maintaining a good documentation and detailed comments inside the code is also key to achieving these goals.

### 3.2 New Structure of the Pattern Generation and Analysis

The structure of the new implementation can be understood by following the steps which are carried out when a measurement is started:

First the function `GenerateQubitCalibPattern` is called by `QubitCalib` or manually. It loads the parameters for the pattern which needs to be generated. It passes these parameters to the pattern generation function for the chosen measurement type and gets symbolic descriptions of the pulse sequences used in the experiment. The descriptions are passed to the generic function `CalculateWaveforms` which returns the numeric waveforms for the pulses. Finally, the binary pattern files for the AWGs are generated from the waveforms and saved.

After the measurement, `QubitCalib` or a user performing a manual analysis calls the function `AnalyzeQubitCalib`. It loads the parameters used in the pattern generation and calls a generic function which reads the raw data from files and returns the populations of the qubit states. The populations are passed to the analysis function for the chosen measurement type. The analysis function returns the new values for physical parameters which need to be updated in the pattern config file, a graphical output consisting of plots of the measurement and text with the new parameter values, and a text-based output with the measurement results. `AnalyzeQubitCalib` writes the new parameters to the pattern config file, exports the graphical

output and returns the measurement results to QubitCalib. The user can see the graphical output on the QubitCalib frontend, perform more analyses with the returned results, and use the updated values in the pattern config to generate pulse sequences for other experiments.

The controller functions `GenerateQubitCalibPattern` and `AnalyzeQubitCalib` are located in the library `QubitCalibSpecific.m`. The pattern generation and analysis functions for similar experiments are collected in libraries. Currently, all functions are collected in two libraries `SingleQubitCalibration.m` and `SingleQubitEFCalibration.m` for measurements on the *ge*-transition and the *ef*-transition respectively.

### 3.3 Adding New Experiment Types

Adding new experiments is greatly simplified in the new framework because only the parts which are specific to the experiment need to be implemented. Everything else, like loading parameters or updating the `pattern config` file, is handled by the two controller functions `GenerateQubitCalibPattern` and `AnalyzeQubitCalib`. When implementing new operations the user does not even need to know the details of the measurement non-specific tasks. The required steps for adding a new operation are:

- Write a pattern generation function which takes the parameters from pattern config as argument and returns a list of symbolic pulse sequence descriptions.
- Write an analysis function which takes the calculated populations, the parameters from the pattern generation, and if necessary the AWG channels which were used as arguments. The return value should be a list `{newParams, graphicOutput, consoleOutput}`.
  - `newParams` is a list `{{name, value, factor}, ...}` of the parameters and values which should be updated in the pattern config file. The string `factor` is used to format the numbers in the pattern config file to be human readable. For example `{"t1", 0.000001, "10^-6"}` will be written to the pattern config file as `t1 = 1*10^-6`.
  - `graphicOutput` is a list of graphics objects and text which will be printed in the log and shown on the QubitCalib frontend. Usually this consists of one or two plots and a text grid with the measured parameters their and values.
  - `consoleOutput` is a list `{{label, value}, ...}` of the measurement results which are returned to QubitCalib. An example result is `{"T1[us]", 1}`.

- Add calls to your new pattern generation and analysis functions in the controller functions `GenerateQubitCalibPattern` and `AnalyzeQubitCalib`.
- Choose the method for calculating the populations in the analysis of your experiment. If your experiment does not use the standard scaling of two populations to the *ge*-contrast as explained in Section 2.2, add it to the switch where the populations are calculated in `AnalyzeQubitCalib`.

Note that `AnalyzeQubitCalib` does not check the values before it writes them to the pattern config file because sanity checks are measurement-specific. Therefore all error handling and sanity checks for the new parameter values must be included in the analysis function.

### 3.4 Outlook

The new framework was only implemented for single qubit operations, so the next step is to extend it to also support multi-qubit operations. Once all the code is organized in libraries, `QubitCalib` can be also be updated: Currently, every time the pattern generation or analysis is called a new Mathematica kernel is started for running a chosen Mathematica notebook. A cleaner way to make use of the new libraries would be to have `QubitCalib` run a single Mathematica kernel with the libraries loaded, and call the controller functions in the same kernel when they are needed. This would also eliminate some of the text-based communication between LabView and the Mathematica kernel because parameters could be stored as variables in the kernel.



## 4 Automatic Single Qubit Routines

QubitCalib has automatic routines to calibrate the gate parameters and characterize the qubit. All physical parameters needed for the pulse generation and some characteristic values of the qubit are stored in the pattern config file. The automatic routines perform measurements to determine the correct parameter values and update them in the pattern config file.

This Chapter is dedicated to explaining the automatic single qubit routines that are now implemented in the new framework. In Sections 4.1 and 4.2 I discuss the characteristics of the control pulses and the routines which calibrate the parameters that describe them. I then discuss the measurements used to characterize the qubit by its coherence time and gate fidelity in Sections 4.3 and 4.4. In Section 4.5 I introduce measurements on the  $ef$ -transition and explain the measurement of the thermal population in the  $|e\rangle$  level as an example application.

### 4.1 Pulse Model

When applying pulses to the qubit we usually want to drive the  $ge$ -transition without affecting other energy levels to avoid leakage of population into states outside the computational space. To achieve this we use Gaussian-like DRAG pulses (Derivative Removal by Adiabatic Gate) which are shaped in a way that frequency components near the  $ef$ -transition frequency  $\omega_{ef}$  are suppressed [Motzoi 09, Gambetta 11]. As shown in the comparison of the power spectra of a Gaussian pulse and a DRAG pulse in Fig. 5, the spectrum of the DRAG pulse has a minimum at  $\omega_{ef}$  where the Gaussian pulse still has a significant contribution.

In our implementation with single-sideband mixing the two quadratures of a DRAG pulse are given by

$$I(t) = A(t) \cos(\omega_{\text{IF}}t + \phi_{\text{IQ}}), \quad (9)$$

$$Q(t) = A(t) \sin(\omega_{\text{IF}}t + \phi_{\text{IQ}}), \quad (10)$$

with the amplitude  $A(t) = \sqrt{\varepsilon_x(t)^2 + \varepsilon_y(t)^2}$  and the phase  $\phi_{\text{IQ}} = \arctan(\varepsilon_y(t)/\varepsilon_x(t))$ . The function  $\varepsilon_x(t)$  is the initial ansatz for the pulse shape and is chosen to be a Gaussian which is truncated at  $3\sigma$  around the maximum and forced to start and end with zero amplitude. The function  $\varepsilon_y(t)$  is given by

$$\varepsilon_y(t) = -\frac{q_s}{\alpha} \frac{d}{dt} \varepsilon_x(t) \quad (11)$$

where  $\alpha$  is the qubit anharmonicity [Baur 12, Gambetta 11]. The QScale factor  $q_s$  is a parameter which needs to be calibrated to optimize the pulse shape for minimal population leakage. In

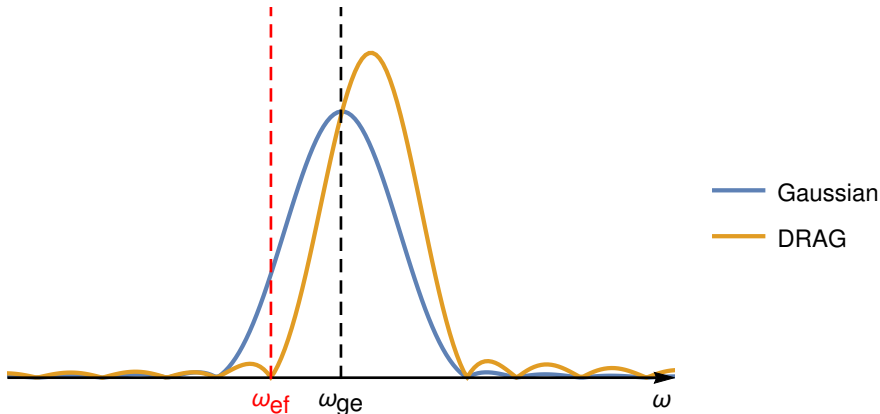


**Figure 5:** Power spectra of a Gaussian pulse and a DRAG pulse on the  $ge$ -transition. The DRAG pulse is optimized to eliminate the frequency components at the  $ef$ -transition frequency  $\omega_{ef}$ .

summary, a DRAG pulse has a fixed length and is characterized by the maximum amplitude, the frequency  $\omega_{IF}$ , and the QScale factor  $q_s$ .

## 4.2 Calibration Experiments

To make a pulse have the desired effect on the qubit state the three parameters that characterize it have to be carefully calibrated. The  $\pi$ -pulse amplitude is found with a Rabi oscillation experiment and the qubit frequency with a Ramsey oscillation experiment. These two experiments and the QScale calibration measurement are explained in this Section, as well as the CalTom experiment used to verify the calibration. A full calibration cycle usually consists of six experiments in the order Rabi–Ramsey–Rabi–QScale–Rabi–CalTom. This is because the  $\pi$ -pulse amplitude changes when the frequency and QScale factor of the pulse are changed.

In a Rabi oscillation experiment a single pulse  $X(\theta)$  is applied and the population is measured as a function of the pulse amplitude. This simple pulse pattern is represented by the pulse scheme in Fig. 6a. In the Bloch sphere picture, the pulse rotates the state vector around the x-axis by an angle  $\theta$ , which is determined by the pulse amplitude. The population oscillates between 0 and 1 as a function of the pulse amplitude or rotation angle, as shown in Fig. 6b. At the maximum of the sine the population has been inverted and therefore the amplitude at this point is the correct amplitude for a  $\pi$ -pulse. The points corresponding to  $\pi$ - and  $\pi/2$ -pulses are marked in Fig. 6b.

The precise resonance frequency of the qubit can be found with a Ramsey oscillation experiment [Ramsey 50]. In this type of experiment two  $\pi/2$ -pulses are applied with a separation  $\tau$  between them. The population is measured directly after the second pulse as a function

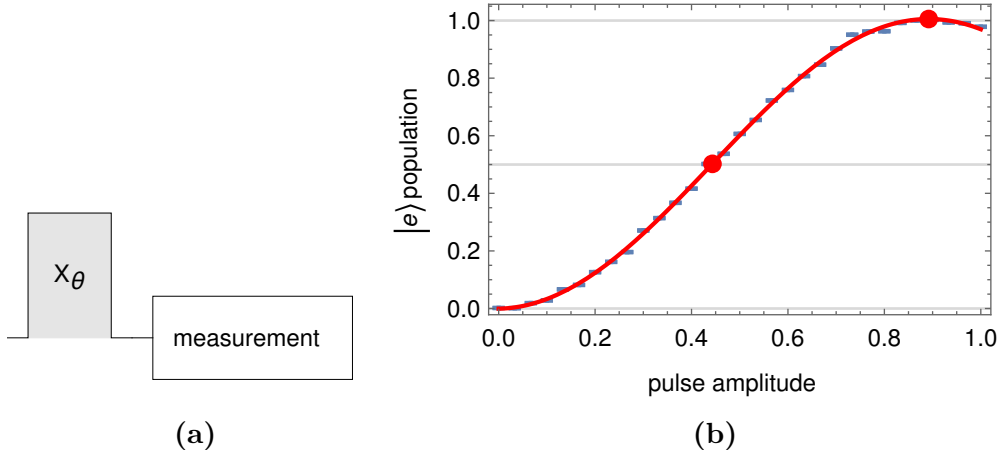


**Figure 6:** (a) Pulse scheme for a Rabi oscillation measurement. A single pulse rotates the state by an angle  $\theta$ . The rotation angle  $\theta$  depends on the amplitude of the pulse. (b) Data and sinusoidal fit curve of a Rabi oscillation measurement. The points corresponding to  $\pi/2$ - and  $\pi$ -pulses are marked.

of the separation  $\tau$ . It oscillates with a frequency equal to the detuning of the drive from the qubit frequency. Additionally, the population decays to 0.5 with a decay constant  $T_2^*$  describing the qubit dephasing [Clarke 08], as shown in Fig. 7b. A single experiment does not give any information about the sign of the detuning. To get the correct sign the experiment is repeated with a different driving frequency and therefore different detuning [Landig 13]. Both data sets are combined in a vector and fitted simultaneously with a two-dimensional model

$$\frac{1}{2} \left( 1 + A \cos((\omega_{ge} + d_1) \tau + \phi_1) e^{-\tau/T_2^*} \right) \cdot \vec{e}_1 + \frac{1}{2} \left( 1 + B \cos((\omega_{ge} + d_2) \tau + \phi_2) e^{-\tau/T_2^*} \right) \cdot \vec{e}_2. \quad (12)$$

The fit parameters are  $\omega_{ge}$ ,  $A$ ,  $B$ ,  $\phi_1$ ,  $\phi_2$ , and  $T_2^*$ , while  $d_1$  and  $d_2$  are the chosen detunings. The fit is done twice: once with same signs for the detunings  $d_1$  and  $d_2$  and once with opposite signs. Only one of them yields a good fit for both data sets and from this fit the qubit frequency is extracted. Additionally, the magnetic flux through the SQUID loop is calculated and the dephasing  $T_2^*$  is extracted from the exponential envelope. The dephasing will be explained in more detail in Section 4.3.

The optimal value for the QScale factor  $q_s$  is found by applying the three pulse sequences  $X(\frac{\pi}{2}) \cdot X(\pi)$ ,  $X(\frac{\pi}{2}) \cdot Y(\pi)$ , and  $X(\frac{\pi}{2}) \cdot -Y(\pi)$  and sweeping the  $q_s$  value. In case of a good calibration all three pulse sequences result in an  $|e\rangle$  population  $p_e = 0.5$ . The value of  $q_s$  for which this is the case is interpolated from the data as shown in Fig. 8.

The calibration is verified with a CalTom measurement. The measured population is compared to the expected for 25 short pulse sequences. The used pulse sequences are given in Fig. 9,

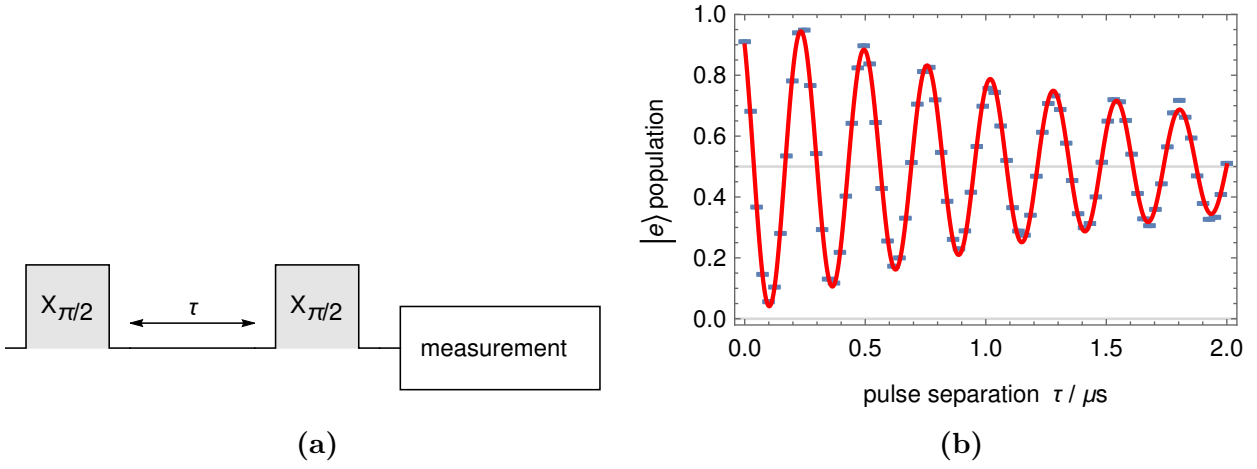


**Figure 7:** (a) Pulse scheme for a Ramsey oscillation measurement. Two  $\pi/2$ -pulses are applied with a separation  $\tau$  between them. The population is measured directly after the second pulse. (a) Data and fit curve of a Ramsey oscillation measurement. The fit function is a sinusoidal oscillation with an exponential envelope.

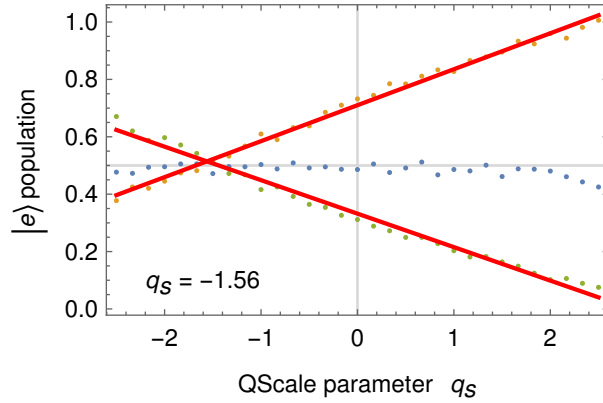


**Figure 8:** Data and linear fits of a QScale calibration measurement. The rising line (orange points) corresponds to the  $X(\frac{\pi}{2}) \cdot Y(\pi)$  sequence, the horizontal line (blue points) to the  $X(\frac{\pi}{2}) \cdot X(\pi)$  sequence, and the falling line (green points) to the  $X(\frac{\pi}{2}) \cdot -Y(\pi)$  sequence. The correct value for  $q_s$  is found from the intersection of the lines.



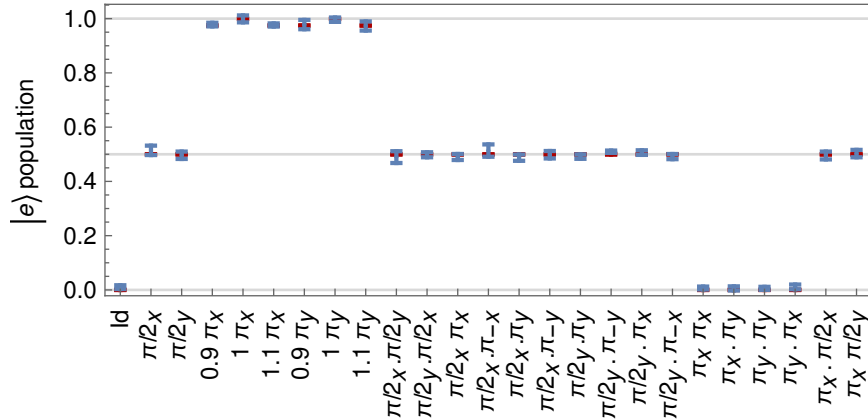


**Figure 9:** Output plot from a CalTom measurement. Twenty-five different pulse sequences are applied and the populations are measured (blue) and compared with the expected populations (red). The points for the expected populations can hardly be seen because they are covered by the measured populations, which means that the qubit is well calibrated.

along with the results of a good calibration. If the calibration was successful, the measured populations do not deviate from the expected.

### 4.3 Coherence Time

The lifetime of a qubit state is characterized by two timescales  $T_1$  and  $T_2$  [Clarke 08]. The longitudinal relaxation  $T_1$  describes the decay of the excited state to the ground state due to energy loss. The transversal relaxation or dephasing  $T_2$  describes the loss of information about the phase of the qubit state. In the Bloch sphere picture, where the computational  $|0\rangle$  and  $|1\rangle$  lie on the z-axis,  $T_1$  describes the relaxation of the z-component of the state vector to its equilibrium state, and  $T_2$  the relaxation of the x- and y-components to 0. The measurements are usually averaged several thousand times to improve the signal-to-noise ratio and obtain a quantum mechanical measurement of the expectation value. Small fluctuations in the qubit frequency during the averaging due to coupling to the environment lead to additional dephasing. This means that a phase decay time  $T_2^* < T_2$  is observed [Clarke 08].

The energy decay  $T_1$  can be measured directly. For this a  $\pi$ -pulse is applied and the population is measured as a function of the separation  $\tau$  between the  $\pi$ -pulse and the measurement. The lifetime  $T_1$  is extracted from an exponential fit to the  $|e\rangle$  population, as shown in Fig. 10.

When measuring the dephasing one must distinguish between the averaged dephasing  $T_2^*$  and the real dephasing  $T_2$ , as explained above. The averaged dephasing is measured in a Ramsey

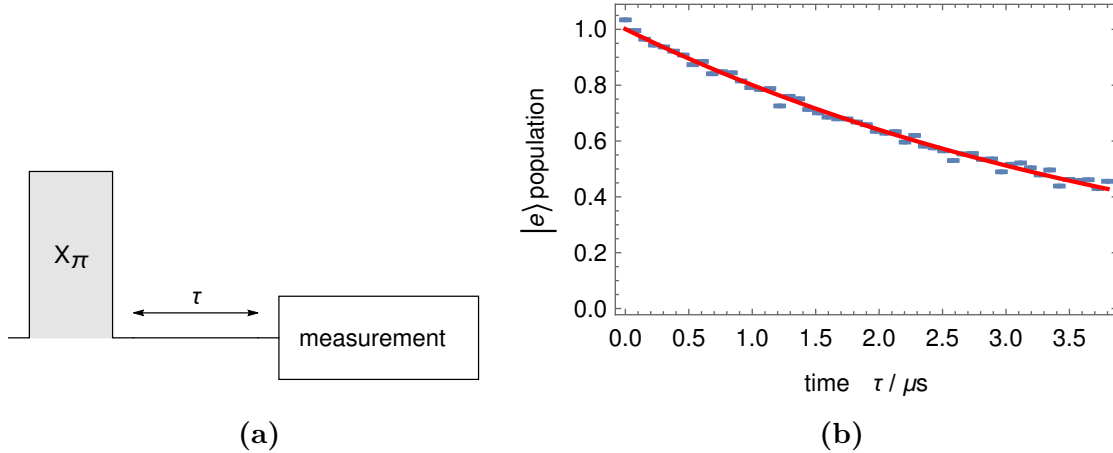


**Figure 10:** (a) Pulse scheme for an energy decay ( $T_1$ ) measurement. The population is measured after a  $\pi$ -pulse and a decay time  $\tau$ . (b) Data and fit of an energy decay measurement. From the exponential fit the mean lifetime  $T_1$  is calculated.

oscillation experiment. Between the two  $\pi/2$ -pulses the state vector lies on the  $xy$ -plane and decays on the timescale  $T_2^*$  because the repetitions of the experiment average over low-frequency noise. The decay constant of the exponential envelope of the oscillation is therefore  $1/T_2^*$  and can be extracted from the fit. To get a better estimate for the dephasing  $T_2$  of a single state the effect of the low-frequency fluctuations in the qubit frequency must be eliminated. This is done with a spin-echo, a technique derived from NMR-spectroscopy [Hahn 50]. The spin-echo pulse sequence is essentially the same as for a Ramsey oscillation measurement, but with an additional  $Y(\pi)$ -pulse in the middle, as shown in Fig. 11. The population is measured as a function of  $\tau$  and decays exponentially with the lifetime  $T_2$ .

A simple explanation for the noise cancelling effect of the spin-echo can be given in the Bloch sphere picture, as shown in Fig. 12: The first  $X(\frac{\pi}{2})$ -pulse rotates the state vector onto the  $y$ -axis. During the first  $\tau/2$  period, the state vector precesses around the  $z$ -axis with a frequency equal to the unknown detuning of the drive from the qubit. The following  $Y(\pi)$ -pulse mirrors the state vector on the  $xz$ -plane, so that after precessing during the second  $\tau/2$  period, the state vector ends up on the  $y$ -axis again, independent of the detuning. The final  $X(\frac{\pi}{2})$ -pulse then rotates the state onto the  $z$ -axis. During the time  $\tau$ , the state vector lies on the  $xy$ -plane and a decay with  $T_2$  is observed. It is measured as a decay of the final population  $p_e$  from 1 to 0.5.

Evidently, the above explanation only holds if the detuning is constant over the time of one pulse sequence. This means that only low-frequency noise can be cancelled with a spin-echo, i. e. fluctuations on a timescale larger than the duration of the individual measurements. The

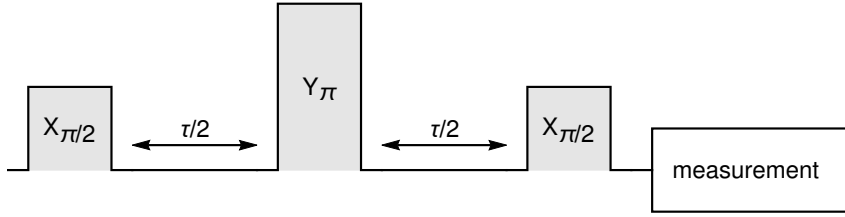


**Figure 11:** Pulse scheme for a dephasing ( $T_2$ ) measurement. Three pulses  $X(\frac{\pi}{2}) \cdot Y(\pi) \cdot X(\frac{\pi}{2})$  are applied, separated by a decay time  $\tau/2$ . The population is measured directly after the third pulse as a function of  $\tau$ .

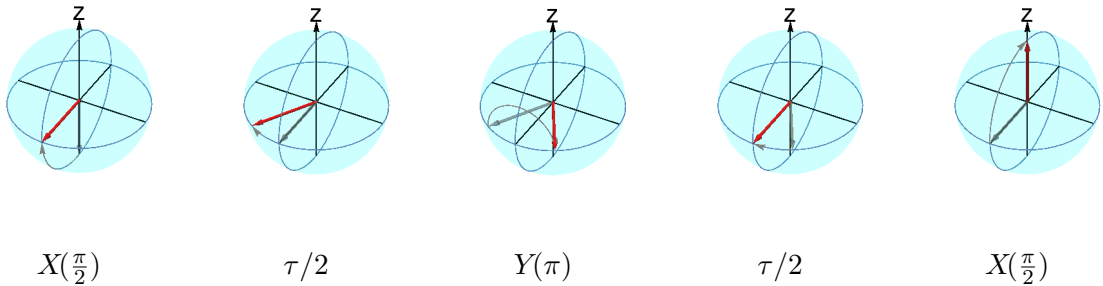


**Figure 12:** Bloch sphere representation of the qubit state during a spin-echo pulse sequence. The state vector is rotated onto the y-axis by the  $X(\frac{\pi}{2})$ -pulse and precesses around the z-axis during the first  $\tau/2$  period. Then it is mirrored on the xz-plane by the  $Y(\pi)$ -pulse and precesses back to the y-axis during the second  $\tau/2$  period. The final  $X(\frac{\pi}{2})$ -pulse rotates the state vector onto the z-axis.

fact that the spin-echo experiment is still sensitive to noise on the same timescale as its duration can be used to probe the noise spectrum [Bylander 11].

## 4.4 Randomized Benchmarking

Due to the limited coherence time of the qubit and imperfections in the pulses, errors accumulate during longer pulse sequences. For scalable quantum computers, the error per gate must be below  $10^{-2}$ , preferably even as low as  $10^{-4}$  [Knill 05, Knill 08]. A good way to find the average error per gate for a qubit is randomized benchmarking [Knill 08]. It enables us to measure the average gate error independent of context, e. g. the position of the gate in a sequence, as well as state preparation and measurement (SPAM) errors.

The idea is to apply pulse sequences of different lengths, compare the final state to the expected outcome, and measure the total fidelity of the output state as a function of the sequence length. The sequences must be randomized to ensure that the result is not dominated by

any particular gate or subsequence. The method was implemented by Lars Steffen [Steffen 13] following the description from the original publication [Knill 08].

- Generate a sequence of randomly chosen  $\pi/2$ -pulses around the x- and y-axes. The length of this sequence is  $l_{\max}$ .
- Create  $N_L$  subsequences with lengths  $l_1 < \dots < l_{N_L} = l_{\max}$  by truncating the original sequence at each of the lengths  $l_i$ .
- Add a final gate to every subsequence such that the final state lies on the z-axis of the Bloch sphere. This ensures that the expected outcome is either  $|g\rangle$  or  $|e\rangle$ .
- From every subsequence create  $N_P$  different randomized sequences by doing  $N_P$  Pauli randomizations. A Pauli randomization is done by adding  $\pi$ -pulses around randomly chosen axes between the  $\pi/2$ -pulses in that subsequence as well as to the start and end of it.
- Apply every randomized sequence to the qubit, measure the outcome, and compare it to the expected outcome. The difference between the expected and measured outcome is the total fidelity of the randomized sequence, i. e. the probability of getting the expected result.

The above steps are repeated  $N_G$  times with different sequences, giving a total of  $N_G N_L N_P$  randomized sequences that are applied to the qubit.

The total fidelity  $F$  decays exponentially to 0.5 as a function of the sequence length  $l$

$$F(l) = \frac{1}{2} (1 + f^{2l}), \quad (13)$$

where  $f$  is the average fidelity of a single rotation. The factor 2 in the exponent arises because the Pauli randomization doubles the length of a sequence. By fitting a model  $1/2(1 + e^{-kl})$  to the data the average error per gate

$$\varepsilon = 1 - f = 1 - e^{-k/2} \quad (14)$$

can be found.

In our setup we measured average errors per gate of about  $\log_{10} \varepsilon = -2.25$ , as shown for example in Fig. 13. This is near the upper limit for the usage in scalable systems according to [Knill 05]. Note that in Fig. 13 the spread of the data points gets very wide for the long sequences. This means that the error is substantially larger in the worst case.

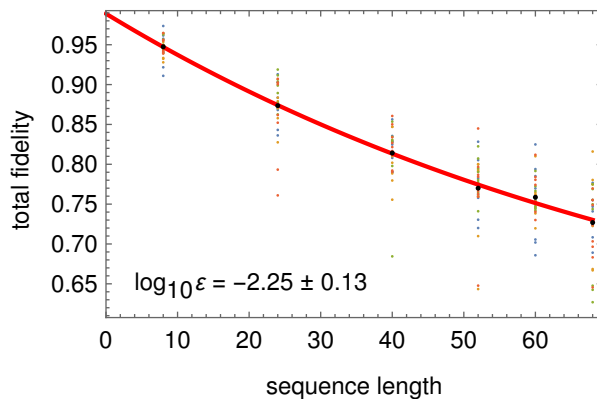


**Figure 13:** Randomized benchmarking experiment. The total fidelity decays exponentially to 0.5 as a function of the sequence length. The average error per gate is calculated from the decay constant.

During the analysis of data from randomized benchmarking experiments we found that sometimes the output  $|e\rangle$  population did not decay to 0.5 as expected. Instead it decayed to a higher value of about 0.7. From the fact that flipping the output state with an additional  $X(\pi)$  pulse did not change the outcome we concluded that there was a problem with the measurement or analysis. The initial analysis was only considering the  $|g\rangle$  and  $|e\rangle$  levels since no other transitions are expected in this experiment. To check for leakage into the  $|f\rangle$  level we performed an analysis where we calculated  $|g\rangle$ ,  $|e\rangle$ , and  $|f\rangle$  populations. The result for a successful randomized benchmarking experiment is shown on the left in Fig. 14, where the  $|f\rangle$  population is always zero and the  $|g\rangle$  and  $|e\rangle$  populations decay symmetrically to 0.5 as expected. In a failed experiment however, some population leaked into the  $|f\rangle$  level, as shown on the right in Fig. 14. The  $|e\rangle$  population thus did not decay to 0.5. Additionally, an analysis that does not take into account the  $|f\rangle$  level will not give the correct populations in this case.

Similar problems with population leakage were not observed in other experiments. The reason is that the  $ef$ -transition is very weakly driven. The leak only became noticeable in randomized benchmarking experiments where long pulse sequences are used that amplify the small amplitude of the  $ef$ -drive.

The leakage of population into the  $|f\rangle$  level arises because the spectral bandwidth of the pulses is greater than the anharmonicity of the qubit. In principle the shape of the DRAG pulses should minimize the driving of the  $ef$ -transition, however it may not always be possible to suppress it completely. In future it is worth considering using longer pulses to address this problem, with the drawback that decoherence effects become stronger. One should also keep

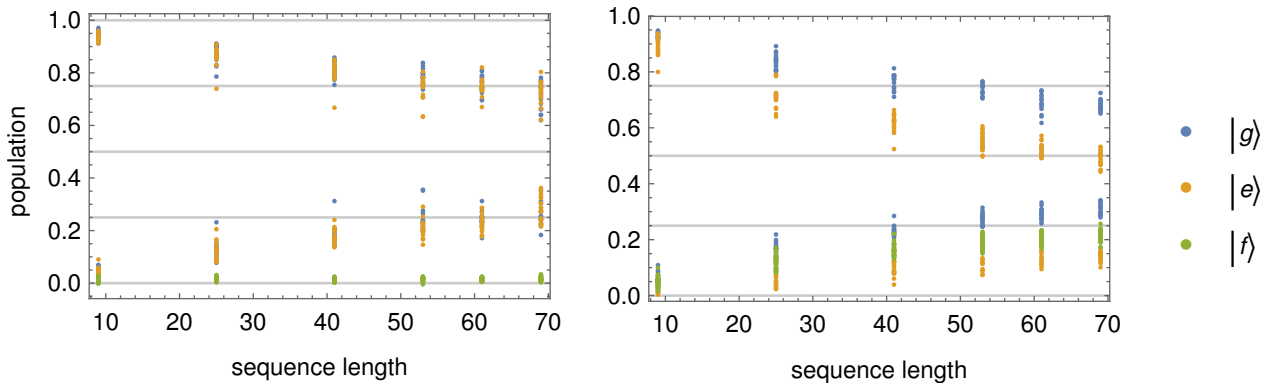


**Figure 14:** Comparison of the  $|g\rangle$ ,  $|e\rangle$ , and  $|f\rangle$  populations in two randomized benchmarking experiments. Left: The  $|f\rangle$  state is never populated and the  $|g\rangle$  and  $|e\rangle$  populations behave as expected. Right: Some population leaks from the  $|e\rangle$  into the  $|f\rangle$  level.

in mind that the population could leak through other channels. In our setup for example the qubit is coupled to two other qubits via resonators.

With the standard randomized benchmarking experiment an estimate of the error averaged over all used gates is obtained. In many cases it is interesting to measure the error of a specific gate. This can be done with a variation of the algorithm called interleaved randomized benchmarking [Magesan 12]. Randomized benchmarking is also extendable to multi-qubit gates [Knill 08, Magesan 11]. An alternative implementation does not use Pauli randomization but chooses pulses randomly from the whole Clifford group [Magesan 11].

For further research it would be interesting to look for the major error sources. A first simple test would be to check if the qubit coherence time or actual pulse errors dominate the total fidelity. Interleaved randomized benchmarking could be used to find gates with high error probability and those errors could be addressed by replacing single pulses with composite pulses [Cummins 03, Vandersypen 04, Ichikawa 11, Ichikawa 14], as it is normal practice in NMR spectroscopy [Levitt 86]. Qubit coherence times can also be increased with pulse techniques derived from NMR [Collin 04], such as the spin-echo described in Section 4.3 [Hahn 50].

## 4.5 $ef$ -transition Experiments

An ideal qubit only has two states  $|0\rangle$  and  $|1\rangle$ . The presence of other states in our physical realization can lead to problems, as seen in Section 4.4. However, there are also applications that make use of the additional energy levels. A simple application that uses the  $|f\rangle$  level is the measurement of the thermal  $|e\rangle$  population, which is discussed in detail below. Another example is to use the  $|f\rangle$ -state to simplify the implementation of a Toffoli gate [Ralph 07, Fedorov 12].

To be able to make use of the  $|f\rangle$  state, pulses that drive the  $ef$ -transition must be calibrated. The experiments used for the  $ef$ -calibration are essentially the same as for the  $ge$ -calibration. However, before every experiment an input state with an initial  $|e\rangle$  population must be prepared. This is done by applying an  $X(\pi)$  pulse on the  $ge$ -transition. The measurement also has to be adjusted, since the decay from  $|f\rangle$  to  $|g\rangle$  is measured. Before the measurement, an additional  $X(\pi)$  pulse is applied on the  $ge$ -transition to put the  $|e\rangle$  population to the  $|g\rangle$  state. The whole population is thus distributed between the  $|g\rangle$  and  $|f\rangle$  states and the  $|f\rangle$  population can be calculated from the resonator transmission difference as usual (see Section 2.3).

The measurement of the energy decay  $T_1^{ef}$  requires an additional adjustment. The reason is that the  $|f\rangle$  level has two decay channels: it can decay to the ground state  $|g\rangle$  either directly or over the  $|e\rangle$  state. The relaxation of the three level system is described by the set of differential equations

$$\frac{d}{dt}f(t) = -(\lambda_{fe} + \lambda_{fg})f(t), \quad (15)$$

$$\frac{d}{dt}e(t) = \lambda_{fe}f(t) - \lambda_{eg}e(t), \quad (16)$$

$$\frac{d}{dt}g(t) = \lambda_{fg}f(t) + \lambda_{eg}e(t). \quad (17)$$

The functions  $f$ ,  $e$ , and  $g$  describe the populations of the three levels. The initial conditions in a  $T_1^{ef}$  experiment are  $f(0) = 1$ ,  $e(0) = g(0) = 0$ . The solution of this system is given by

$$f(t) = e^{-(\lambda_{fe} + \lambda_{fg})t}, \quad (18)$$

$$e(t) = \frac{\lambda_{fe}}{\lambda_{fe} + \lambda_{fg} - \lambda_{eg}} \left( e^{-\lambda_{eg}t} - e^{-(\lambda_{fe} + \lambda_{fg})t} \right), \quad (19)$$

$$g(t) = 1 - \frac{\lambda_{fe}}{\lambda_{fe} + \lambda_{fg} - \lambda_{eg}} e^{-\lambda_{eg}t} - \frac{\lambda_{fg} - \lambda_{eg}}{\lambda_{fe} + \lambda_{fg} - \lambda_{eg}} e^{-(\lambda_{fe} + \lambda_{fg})t}. \quad (20)$$

To analyze the  $T_1^{ef}$  experiment the populations of all three energy levels are calculated. The  $|e\rangle$  and  $|f\rangle$  populations are combined in a vector and fitted simultaneously with a two-dimensional model

$$Ae^{-\Lambda_f\tau}\vec{e}_f + \left( Be^{-\lambda_{eg}\tau} - Ce^{-\Lambda_f\tau} \right)\vec{e}_e. \quad (21)$$

In this model the total decay rate  $\Lambda_f = \lambda_{fe} + \lambda_{fg}$  is used as a fit parameter because the two rates  $\lambda_{fe}$  and  $\lambda_{fg}$  are strongly correlated and hard to fit. The third decay rate  $\lambda_{eg} = 1/T_1^{ge}$  is fixed at the value known from the  $ef$ -calibration. The model describes the data fairly well, as shown in Fig. 15.

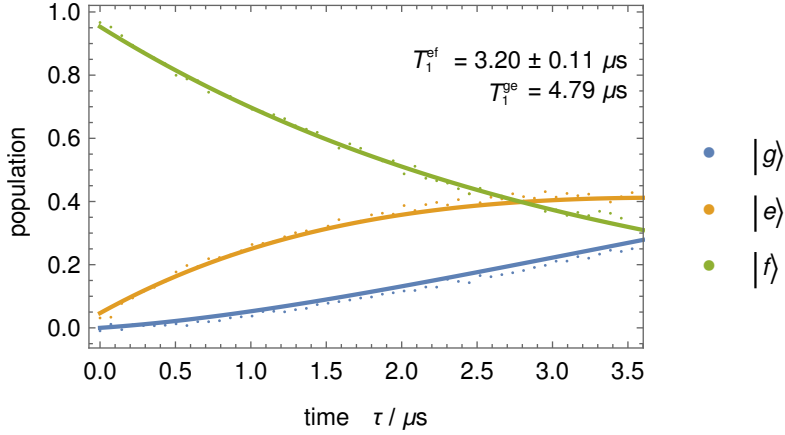


**Figure 15:** Data and fit for a  $T_1^{ef}$  measurement. The total decay constant  $\Lambda_f = \lambda_{fe} + \lambda_{fg}$  of the  $|f\rangle$  state is fitted and the  $\lambda_{eg} = 1/T_1^{ge}$  is fixed at the value known from the  $ge$ -calibration.

The calibration experiments for the  $ef$ -transition are available in QubitCalib as automatic routines. Additionally, we added an automatic measurement of the thermal  $|e\rangle$  population. This measurement is useful because it gives information about the effective temperature that the qubit sees. The effective temperature is raised by electrical noise which passes through the filters in the cabling and is therefore higher than the base temperature of 20 mK provided by the cryostat.

The thermal population is measured by driving two Rabi oscillations on the  $ef$ -transition as shown in Fig. 16 [Geerlings 13]. Since the experiments start from the thermal equilibrium, we can assume that the initial states are fully classical. In this case the amplitude of a Rabi oscillation is proportional to the difference of the initial populations in the levels between which the oscillation is driven. In the first of the two experiments, the  $|g\rangle$  and  $|e\rangle$  state populations are swapped with a  $\pi$ -pulse on the  $ge$ -transition before applying the Rabi pulses. The amplitude of the first Rabi oscillation is therefore  $A_1 = F - G = F - (1 - E - F)$ , where  $G$ ,  $E$ , and  $F$  are the equilibrium populations of the  $|g\rangle$ ,  $|e\rangle$ , and  $|f\rangle$  states, respectively. In the second experiment there is no initial  $\pi^{ge}$ -pulse and the Rabi oscillation is measured directly on the thermal equilibrium state, such that the amplitude is given by  $A_2 = F - E$ . The equilibrium populations are given by the Boltzmann distribution

$$E = e^{-\frac{\hbar\omega_{ge}}{k_B T_{\text{eff}}}}, \quad (22)$$

$$F = e^{-\frac{\hbar(\omega_{ge} + \omega_{ef})}{k_B T_{\text{eff}}}}, \quad (23)$$



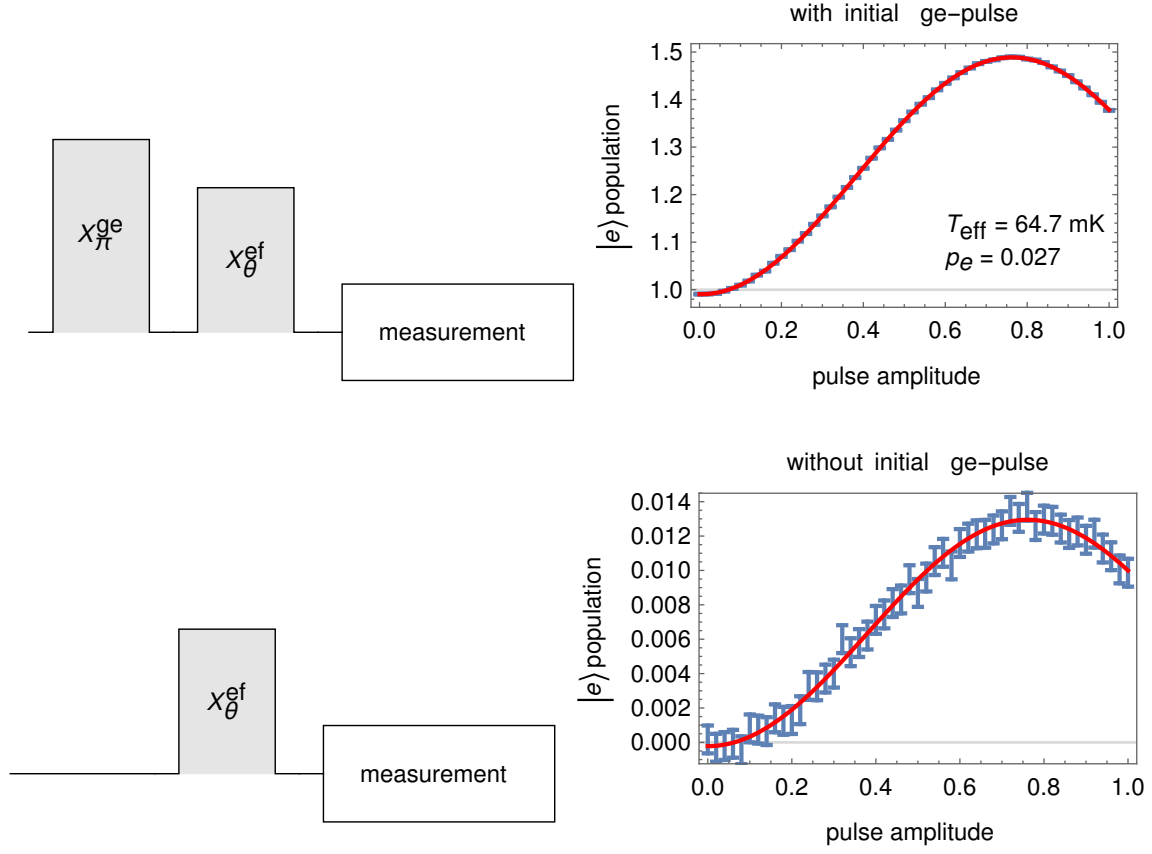


**Figure 16:** Pulse schemes, data and fits for a thermal population measurement. On the top is the Rabi experiment with an initial  $ge$ -pulse, on the bottom the one without the initial  $ge$ -pulse. Note that the units on the  $y$ -axes are scaled to the  $ge$ -transition in both plots. The thermal population is calculated from the ratio of the oscillation amplitudes.

where  $\omega_{ge}$  and  $\omega_{ef}$  are the transition frequencies of the qubit. The effective temperature  $T_{\text{eff}}$  of the qubit can be found by solving

$$\frac{A_2}{A_1} = \frac{E - F}{G - F} = \frac{E - F}{1 - E - 2F} \quad (24)$$

numerically for  $T_{\text{eff}}$ .



## 5 Summary

The software suite that was originally developed in the Quantum Device Lab to automatically run qubit calibration routines is now also used to run other types of experiments. This was a motivation to rethink the design of the software in order to make it easily extendable. In a first step we implemented a new framework for the Wolfram Mathematica component of the software by moving from individual scripts for every experiment type to functions which are organized in libraries. We implemented the standard calibration routines in the new framework as well as a few new experiments to characterize the qubit. We discussed the characterization by the coherence time and with randomized benchmarking and also the use of the  $|f\rangle$  level. Along the road we found that there is a problem with population leaking into the  $|f\rangle$  level in long pulse sequences. We considered using longer pulses with a smaller spectral bandwidth to address this problem.



## Acknowledgements

I would like to thank Andreas Wallraff and the members of the QuDev Lab for the possibility to write my Bachelor thesis in their group and giving me an insight in the interesting field of quantum computing. My special thanks go to my supervisor Johannes Heinsoo who helped and motivated me during the time we worked together, and with whom I had some interesting discussions. Even though I do not know them personally I would also like to thank Matthias Baur, Andreas Landig, Tim Menke, and Lars Steffen who's work mine is based on [Baur 12, Menke 13, Landig 13, Steffen 13].



## References

- [Baur 12] Matthias Baur. *Realizing quantum gates and algorithms with three superconducting qubits*. PhD thesis, ETH Zurich, 03 2012. 3, 4, 5, 6, 8, 15, 31
- [Bianchetti 09] R. Bianchetti, S. Filipp, M. Baur, J. M. Fink, M. Göppl, P. J. Leek, L. Steffen, A. Blais & A. Wallraff. *Dynamics of dispersive single-qubit readout in circuit quantum electrodynamics*. Phys. Rev. A, vol. 80, no. 4, pages 043840–7, 2009. 6
- [Bianchetti 10] R. Bianchetti, S. Filipp, M. Baur, J. M. Fink, C. Lang, L. Steffen, M. Boissonneault, A. Blais & A. Wallraff. *Control and Tomography of a Three Level Superconducting Artificial Atom*. Phys. Rev. Lett., page 223601, Nov 2010. 6
- [Blais 04] A. Blais, R.-S. Huang, A. Wallraff, S. M. Girvin & R. J. Schoelkopf. *Cavity quantum electrodynamics for superconducting electrical circuits: An architecture for quantum computation*. Phys. Rev. A, vol. 69, no. 6, pages 062320–14, June 2004. 5, 6
- [Blais 07] A. Blais, J. Gambetta, A. Wallraff, D. I. Schuster, S. M. Girvin, M. H. Devoret & R. J. Schoelkopf. *Quantum-information processing with circuit quantum electrodynamics*. Phys. Rev. A, vol. 75, no. 3, pages 032329–21, March 2007. 6
- [Blatt 12] R. Blatt & C.F. Roos. *Quantum simulations with trapped ions*. Nat. Phys., vol. 8, pages 277–284, 2012. 1
- [Büttiker 87] M. Büttiker. *Zero-current persistent potential drop across small-capacitance Josephson junctions*. Phys. Rev. B, vol. 36, no. 7, pages 3548–3555, Sep 1987. 3
- [Bylander 11] J. Bylander, S. Gustavsson, F. Yan, F. Yoshihara, K. Harrabi, G. Fitch, D. G. Cory, Y. Nakamura, J.-S. Tsai & Oliver W. D. *Noise spectroscopy through dynamical decoupling with a superconducting flux qubit*. Nat. Phys., vol. 7, pages 565–570, 2011. 21
- [Cirac 95] J. I. Cirac & P. Zoller. *Quantum Computations with Cold Trapped Ions*. Phys. Rev. Lett., vol. 74, pages 4091–4094, May 1995. 1

- [Clarke 08] John Clarke & Frank K. Wilhelm. *Superconducting quantum bits*. Nature, vol. 453, no. 7198, pages 1031–1042, June 2008. 17, 19
- [Collin 04] E. Collin, G. Ithier, A. Aassime, P. Joyez, D. Vion & D. Esteve. *NMR-like control of a quantum bit superconducting circuit*. Phys. Rev. Lett., vol. 93, no. 15, pages 157005–4, October 2004. 24
- [Cory 97] David G. Cory, Amr F. Fahmy & Timothy F. Havel. *Ensemble quantum computing by NMR spectroscopy*. Proceedings of the National Academy of Sciences, vol. 94, no. 5, pages 1634–1639, March 1997. 1
- [Cottet 02] A. Cottet. *Implementation of a quantum bit in a superconducting circuit*. PhD thesis, Université Paris 6, 2002. 3
- [Cummins 03] Holly K. Cummins, Gavin Llewellyn & Jonathan A. Jones. *Tackling systematic errors in quantum logic gates with composite rotations*. Phys. Rev. A, vol. 67, page 042308, Apr 2003. 24
- [Deutsch 85] D. Deutsch. *Quantum Theory, the Church-Turing Principle and the Universal Quantum Computer*. Proceedings of the Royal Society of London. Series A, Mathematical and Physical Sciences, vol. 400, no. 1818, pages 97–117, July 1985. 1
- [Deutsch 92] David Deutsch & Richard Jozsa. *Rapid Solution of Problems by Quantum Computation*. Proceedings: Mathematical and Physical Sciences, vol. 439, no. 1907, pages 553–558, December 1992. 1
- [DiVincenzo 00] D. P. DiVincenzo. *The Physical Implementation of Quantum Computation*. Fortschritte der Physik, vol. 48, no. 9-11, pages 771–783, 2000. 3
- [Fedorov 12] A. Fedorov, L. Steffen, M. Baur, M. P. da Silva & A. Wallraff. *Implementation of a Toffoli gate with superconducting circuits*. Nature, vol. 481, no. 7380, pages 170–172, jan 2012. 24
- [Feynman 82] Richard P. Feynman. *Simulating physics with computers*. Int. J. Theor. Phys., vol. 21, no. 6, pages 467–488, June 1982. 1
- [Filipp 09] S. Filipp, P. Maurer, P. J. Leek, M. Baur, R. Bianchetti, J. M. Fink, M. Göppl, L. Steffen, J. M. Gambetta, A. Blais & A. Wallraff. *Two-*



- Qubit State Tomography Using a Joint Dispersive Readout.* Phys. Rev. Lett., vol. 102, no. 20, page 200402, 2009. 6
- [Friedenauer 08] A. Friedenauer, H. Schmitz, J. T. Glueckert, D. Porras & T. Schaetz. *Simulating a quantum magnet with trapped ions.* Nat. Phys., vol. 4, page 757, July 2008. 1
- [Gambetta 11] J. M. Gambetta, F. Motzoi, S. T. Merkel & F. K. Wilhelm. *Analytic control methods for high-fidelity unitary operations in a weakly nonlinear oscillator.* Phys. Rev. A, vol. 83, no. 1, pages 012308–13, January 2011. 15
- [Geerlings 13] K. Geerlings, Z. Leghtas, I. M. Pop, S. Shankar, L. Frunzio, R. J. Schoelkopf, M. Mirrahimi & M. H. Devoret. *Demonstrating a Driven Reset Protocol for a Superconducting Qubit.* Phys. Rev. Lett., vol. 110, page 120501, Mar 2013. 26
- [Georgescu 14] I. M. Georgescu, S. Ashhab & F. Nori. *Quantum Simulation.* Rev. Mod. Phys., 2014. 1
- [Gershenfeld 97] N. Gershenfeld & I. Chuang. *Bulk Spin Resonance Quantum Computation.* Science, vol. 275, pages 350–356, 1997. 1
- [Gilowski 08] M. Gilowski, T. Wendrich, T. Müller, Ch. Jentsch, W. Ertmer, E. M. Rasel & W. P. Schleich. *Gauss Sum Factorization with Cold Atoms.* Phys. Rev. Lett., vol. 100, page 030201, Jan 2008. 1
- [Grover 96] Lov K. Grover. *A fast quantum mechanical algorithm for database search.* In Proceedings of the twenty-eighth annual ACM symposium on Theory of computing, pages 212–219, Philadelphia, Pennsylvania, United States, 1996. ACM. 1
- [Hahn 50] E. L. Hahn. *Spin Echoes.* Phys. Rev., vol. 80, pages 580–594, Nov 1950. 20, 24
- [Heinsoo 13] Johannes Heinsoo. Automatic multi-qubit gate calibration. Master’s thesis, ETH Zurich, 06 2013. 2, 10
- [Ichikawa 11] Tsubasa Ichikawa, Masamitsu Bando, Yasushi Kondo & Mikio Nakahara. *Designing robust unitary gates: Application to concatenated composite pulses.* Phys. Rev. A, vol. 84, page 062311, Dec 2011. 24

- [Ichikawa 14] Tsubasa Ichikawa, Jefferson G. Filgueiras, Masamitsu Bando, Yasushi Kondo, Mikiyo Nakahara & Dieter Suter. *Construction of arbitrary robust one-qubit operations using planar geometry*. Phys. Rev. A, vol. 90, page 052330, Nov 2014. 24
- [Jaynes 63] E.T. Jaynes & F.W. Cummings. *Comparison of quantum and semiclassical radiation theories with application to the beam maser*. Proceedings of the IEEE, vol. 51, no. 1, pages 89–109, 1963. 5
- [Josephson 62] B. D. Josephson. *Possible new effects in superconductive tunnelling*. Physics Letters, vol. 1, no. 7, pages 251–253, July 1962. 3
- [Kim 10] K. Kim, M.-S. Chang, S. Korenblit, R. Islam, E. E. Edwards, J. K. Freericks, G.-D. Lin, L.-M. Duan & C. Monroe. *Quantum simulation of frustrated Ising spins with trapped ions*. Nature, vol. 465, no. 7298, pages 590–593, June 2010. 1
- [Knill 01] E. Knill, R. Laflamme & G. J. Milburn. *A scheme for efficient quantum computation with linear optics*. Nature, vol. 409, no. 6816, pages 46–52, January 2001. 1
- [Knill 05] E. Knill. *Quantum computing with realistically noisy devices*. Nature, vol. 434, no. 7029, pages 39–44, March 2005. 21, 22
- [Knill 08] E. Knill, D. Leibfried, R. Reichle, J. Britton, R. B. Blakestad, J. D. Jost, C. Langer, R. Ozeri, S. Seidelin & D. J. Wineland. *Randomized benchmarking of quantum gates*. Phys. Rev. A, vol. 77, page 012307, Jan 2008. 21, 22, 24
- [Koch 07] Jens Koch, Terri M. Yu, Jay Gambetta, A. A. Houck, D. I. Schuster, J. Majer, Alexandre Blais, M. H. Devoret, S. M. Girvin & R. J. Schoelkopf. *Charge-insensitive qubit design derived from the Cooper pair box*. Phys. Rev. A, vol. 76, no. 4, page 042319, 2007. 2, 3, 5, 6
- [Landig 13] Andreas Landig. Software for arbitrary single qubit and qutrit gate calibration. Master’s thesis, ETH Zurich, 11 2013. 2, 17, 31
- [Lang 14] Christian Lang. *Quantum Microwave Radiation and its Interference Characterized by Correlation Function Measurements in Circuit Quantum Electrodynamics*. PhD thesis, ETH Zurich, 02 2014. 6

- [Lanyon 11] B. P. Lanyon, C. Hempel, D. Nigg, M. Müller, R. Gerritsma, F. Zähringer, P. Schindler, J. T. Barreiro, M. Rambach, G. Kirchmair, M. Hennrich, P. Zoller, R. Blatt & C. F. Roos. *Universal Digital Quantum Simulation with Trapped Ions*. *Science*, vol. 334, no. 6052, pages 57–61, 2011. 1
- [Levitt 86] Malcolm H. Levitt. *Composite pulses*. *Progress in Nuclear Magnetic Resonance Spectroscopy*, vol. 18, no. 2, pages 61 – 122, 1986. 24
- [Loss 98] Daniel Loss & David P. DiVincenzo. *Quantum computation with quantum dots*. *Phys. Rev. A*, vol. 57, no. 1, pages 120–, January 1998. 1
- [Magesan 11] Easwar Magesan, J. M. Gambetta & Joseph Emerson. *Scalable and Robust Randomized Benchmarking of Quantum Processes*. *Phys. Rev. Lett.*, vol. 106, page 180504, May 2011. 24
- [Magesan 12] Easwar Magesan, Jay M. Gambetta, B. R. Johnson, Colm A. Ryan, Jerry M. Chow, Seth T. Merkel, Marcus P. da Silva, George A. Keefe, Mary B. Rothwell, Thomas A. Ohki, Mark B. Ketchen & M. Steffen. *Efficient Measurement of Quantum Gate Error by Interleaved Randomized Benchmarking*. *Phys. Rev. Lett.*, vol. 109, page 080505, Aug 2012. 24
- [Majer 07] J. Majer, J. M. Chow, J. M. Gambetta, J. Koch, B. R. Johnson, J. A. Schreier, L. Frunzio, D. I. Schuster, A. A. Houck, A. Wallraff, A. Blais, M. H. Devoret, S. M. Girvin & R. J. Schoelkopf. *Coupling superconducting qubits via a cavity bus*. *Nature*, vol. 449, no. 7161, pages 443–447, September 2007. 7
- [Menke 13] Tim Menke. Realizing a calibration program for superconducting qubits. Master’s thesis, ETH Zurich, 08 2013. 2, 31
- [Motzoi 09] F. Motzoi, J. M. Gambetta, P. Rebentrost & F. K. Wilhelm. *Simple Pulses for Elimination of Leakage in Weakly Nonlinear Qubits*. *Phys. Rev. Lett.*, vol. 103, no. 11, page 110501, 2009. 15
- [Neumann 10] P. Neumann, R. Kolesov, B. Naydenov, J. Beck, F. Rempp, M. Steiner, V. Jacques, G. Balasubramanian, M. L. Markham, D. J. Twitchen, S. Pez-zagna, J. Meijer, J. Twamley, F. Jelezko & J. Wrachtrup. *Quantum register based on coupled electron spins in a room-temperature solid*. *Nat. Phys.*, vol. 6, no. 4, pages 249–253, April 2010. 1

- [Nielsen 00] Michael A. Nielsen & Isaac L. Chuang. *Quantum computation and quantum information*. Cambridge University Press, 2000. 1
- [Politi 09] Alberto Politi, Jonathan C. F. Matthews & Jeremy L. O’Brien. *Shor’s Quantum Factoring Algorithm on a Photonic Chip*. *Science*, vol. 325, page 1221, 2009. 1
- [Ralph 07] T. C. Ralph, K. J. Resch & A. Gilchrist. *Efficient Toffoli gates using qudits*. *Phys. Rev. A*, vol. 75, page 022313, 2007. 24
- [Ramsey 50] Norman F. Ramsey. *A Molecular Beam Resonance Method with Separated Oscillating Fields*. *Phys. Rev.*, vol. 78, pages 695–699, Jun 1950. 16
- [Salathé 15] Y. Salathé, M. Mondal, M. Oppliger, J. Heinsoo, P. Kurpiers, A. Potočnik, A. Mezzacapo, U. Las Heras, L. Lamata, E. Solano, S. Filipp & A. Wallraff. *Digital Quantum Simulation of Spin Models with Circuit Quantum Electrodynamics*. *Phys. Rev. X*, vol. 5, page 021027, 06 2015. 1
- [Shor 97] Peter W. Shor. *Polynomial-Time Algorithms for Prime Factorization and Discrete Logarithms on a Quantum Computer*. *SIAM Journal on Scientific and Statistical Computing*, vol. 26, page 1484, 1997. 1
- [Steffen 13] Lars Steffen. *Quantum Teleportation and Efficient Process Verification with Superconducting Circuits*. PhD thesis, ETH Zurich, 2013. 22, 31
- [Vandersypen 01] Lieven M. K. Vandersypen, Matthias Steffen, Gregory Breyta, Costantino S. Yannoni, Mark H. Sherwood & Isaac L. Chuang. *Experimental realization of Shor’s quantum factoring algorithm using nuclear magnetic resonance*. *Nature*, vol. 414, page 883, 2001. 1
- [Vandersypen 04] L. M. K. Vandersypen & I. L. Chuang. *NMR techniques for quantum control and computation*. *Rev. Mod. Phys.*, vol. 76, page 1037, 2004. 24
- [Wallraff 04] A. Wallraff, D. I. Schuster, A. Blais, L. Frunzio, R.-S. Huang, J. Majer, S. Kumar, S. M. Girvin & R. J. Schoelkopf. *Strong coupling of a single photon to a superconducting qubit using circuit quantum electrodynamics*. *Nature*, vol. 431, pages 162–167, 2004. 5
- [Wiesner 83] Stephen Wiesner. *Conjugate Coding*. *SIGACT News*, vol. 15, no. 1, pages 78–88, January 1983. 1

[Zagoskin 07] Alexandre Zagoskin & Alexandre Blais. Physics in canada / la physique au canada, volume 63, pages 215–227. CAP, 2007. 1



# A Input and Output of Automatic Routines

This appendix serves as a documentation for developers in the QuDev Lab. It contains a table with the parameters from the pattern config file needed for the pattern generation and updated during the analysis of every implemented single qubit routine. Additionally, it contains example output plots for selected routines.

## A.1 Input and Output Parameters

Type	Input parameters	Updated parameters
Rabi	rabi_min_amplitude rabi_max_amplitude rabi_points	pi_amp pihalf_amp
Ramsey	ramsey_detuning1 ramsey_detuning2 ramsey_min_separation ramsey_max_separation ramsey_points	if_freq qubitFrequency [ <i>qubitNumber</i> ] t2 fluxOffsetsParking
QScale	qscale_min qscale_max qscale_points	qscale
T1	t1_min_separation t1_max_separation t1_points	t1
T2	t2_min_separation t2_max_separation t2_points	real_t2
CalTom		
RBPauli	RBPauli_NG RBPauli_NP RBPauli_lengths	
RabiEF	rabi_ef_min_amplitude rabi_ef_max_amplitude rabi_ef_points	pi_amp_ef pihalf_amp_ef
RamseyEF	ramsey_ef_detuning1 ramsey_ef_detuning2	if_freq_ef qubit_anharmonicity

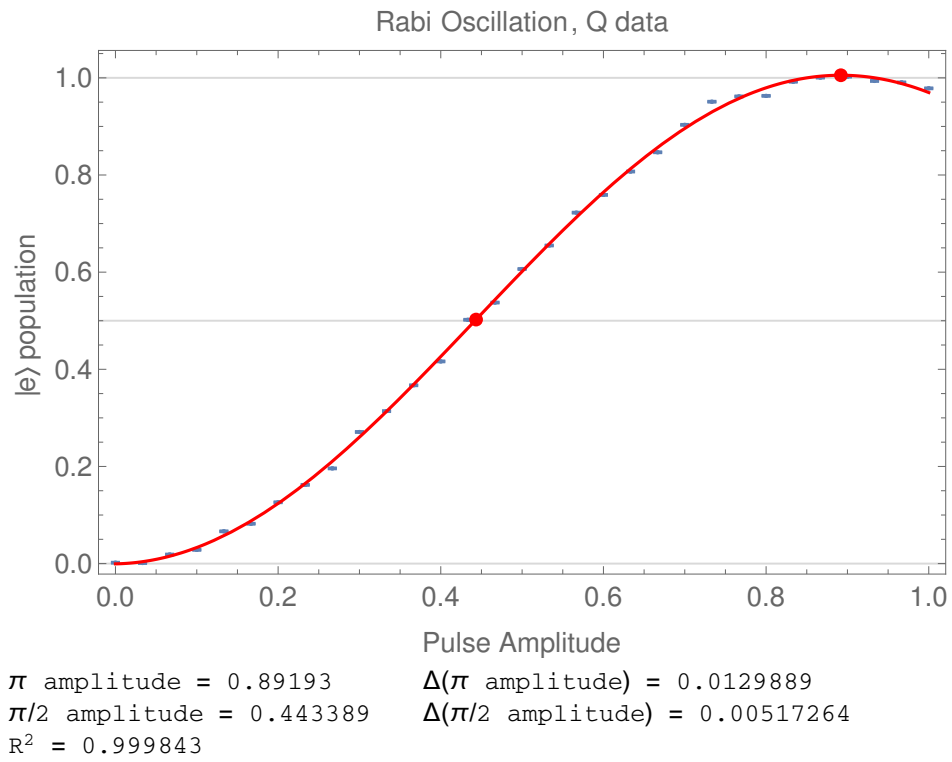
Type	Input parameters	Updated parameters
	ramsey_ef_min_separation ramsey_ef_max_separation ramsey_ef_points	t2_ef
QScaleEF	qscale_ef_min qscale_ef_max qscale_ef_points	qscale_ef
T1EF	t1_ef_min_separation t1_ef_max_separation t1_ef_points	t1_ef
T2EF	t2_ef_min_separation t2_ef_max_separation t2_ef_points	real_t2_ef
CalTomEF		
ThermalPop	rabi_ef_min_amplitude rabi_ef_max_amplitude rabi_ef_points	



## A.2 Example Graphical Output of QubitCalib

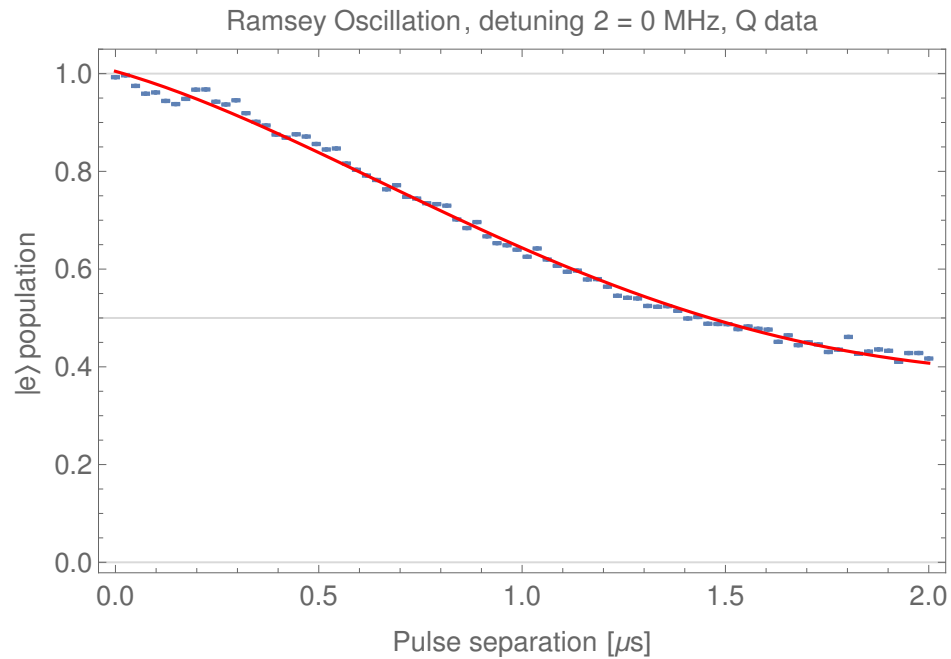
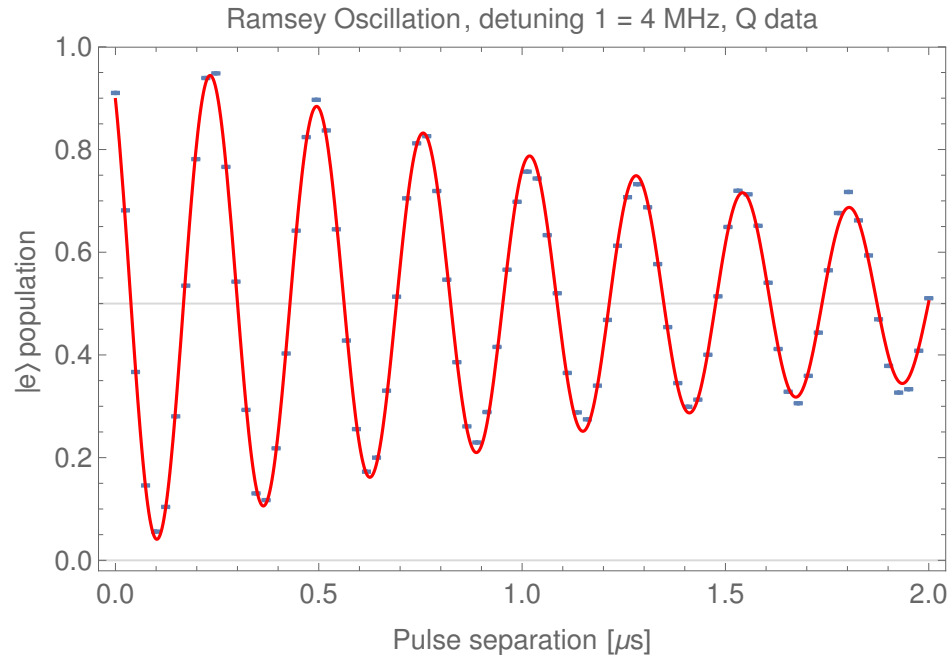
Wed 29 Apr 2015 14:59:25

### 1433\_Rabi\_Qb1



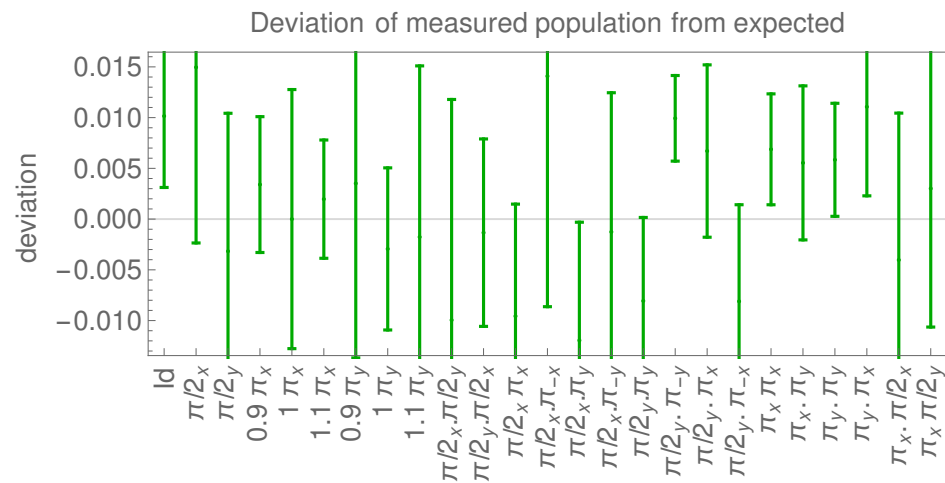
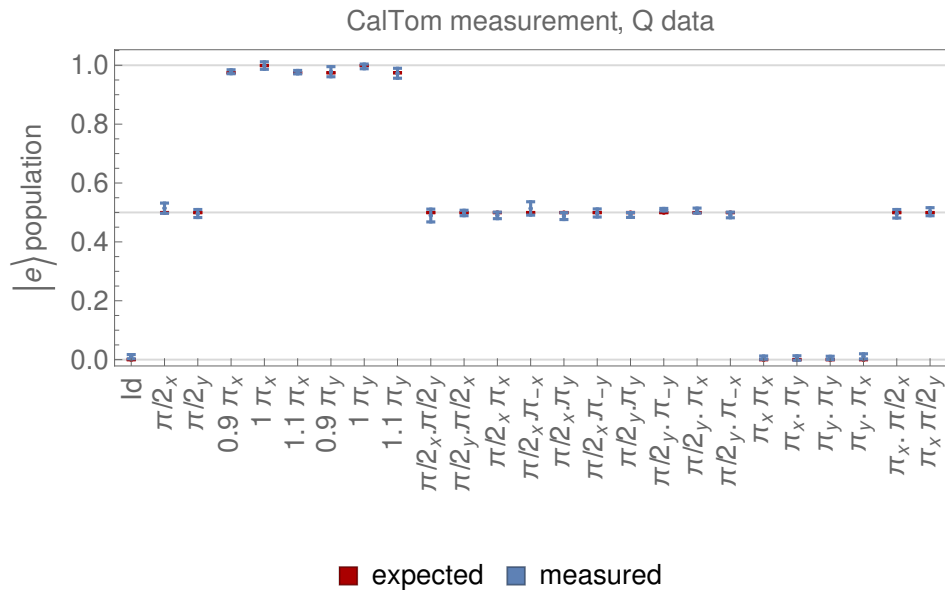
Fri 5 Jun 2015 13:18:46

## 1228\_Ramsey2F\_Qb1



IF [MHz] = $96.725 \pm 0.00203672$	$\Delta$ IF [MHz] = 0.175
$T_2^*$ [ $\mu$ s] = $1.75756 \pm 0.0416296$	$\Delta T_2^*$ [ $\mu$ s] = 0.281885
Q1 frequency [GHz] = 5.44928	
Flux [ $\Phi_0$ ] = 0.0792862	$\Delta$ Flux [ $\Phi_0$ ] = 0.0000764394
$R^2 = 0.999548$	

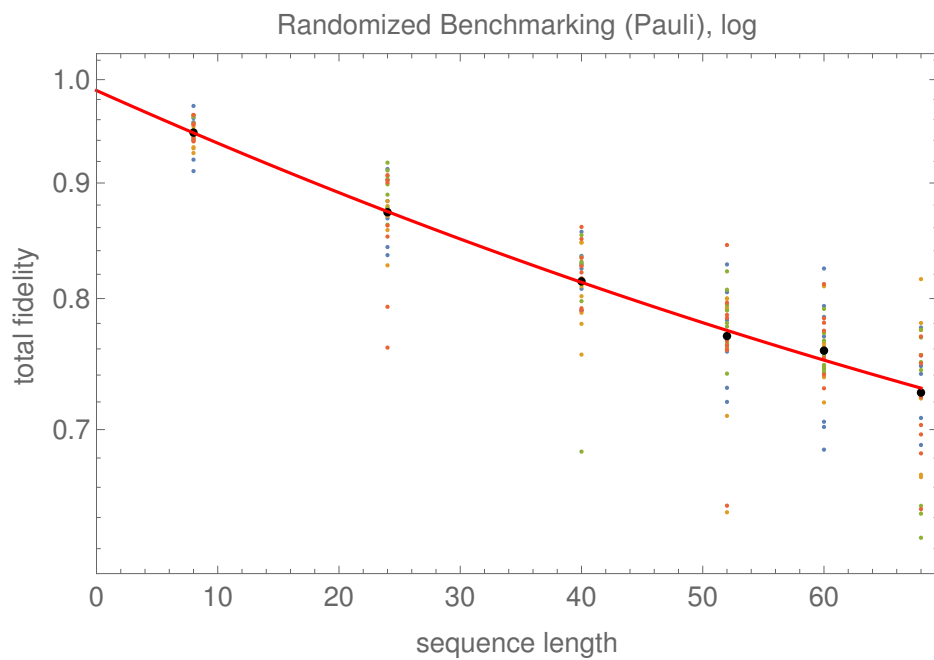
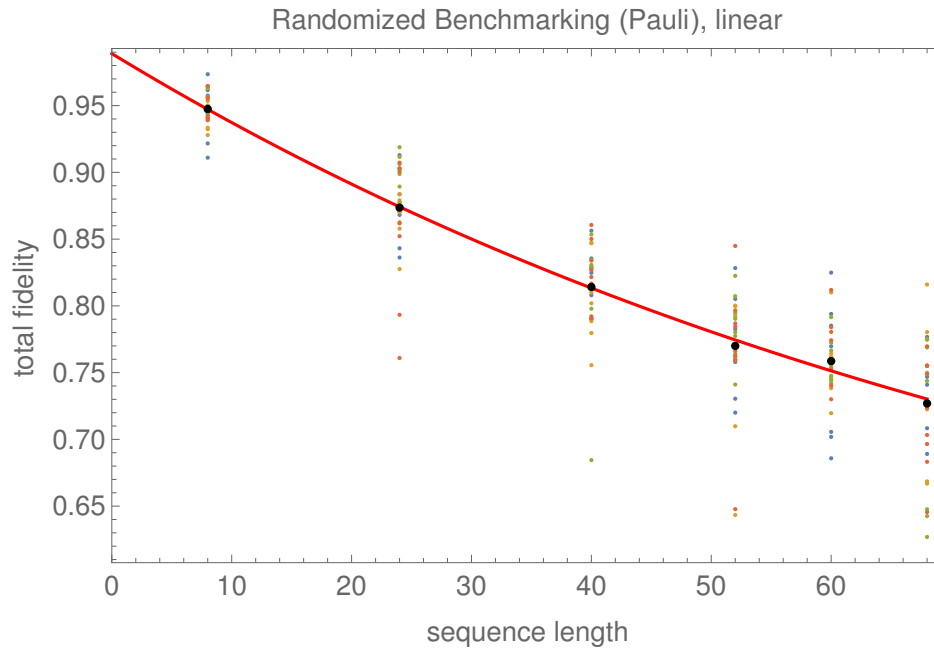
# 1018\_CalTom\_Qb2



Maximal  $|e\rangle$  population: 0.999058 with pulse:  $1 \pi_x$   
 $\pi_x$  pulse population: 0.999058  
 $\pi_y$  pulse population: 0.996119

Wed 27 May 2015 09:31:42

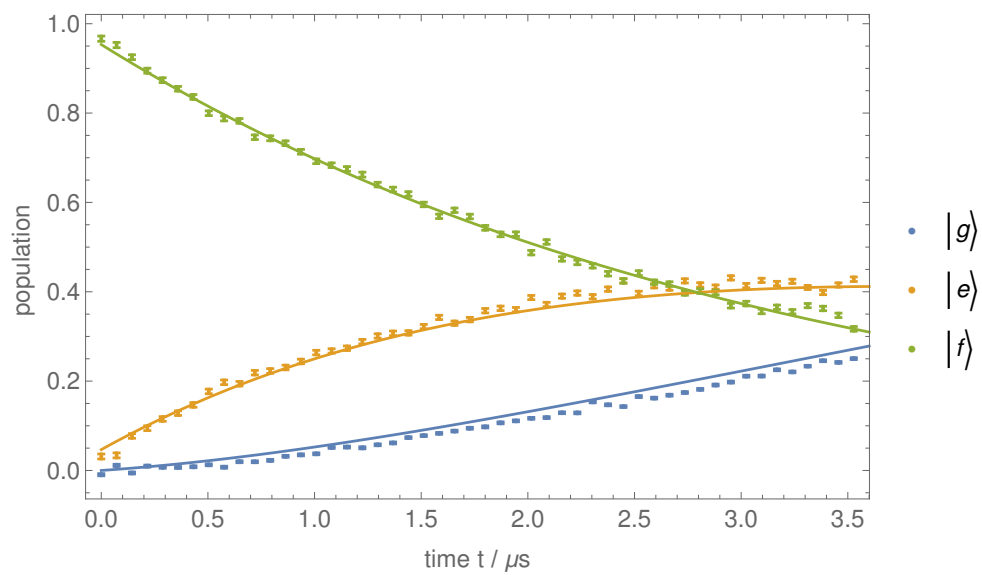
## 1590\_RBPauliGate\_RBPauli\_Qb3



$\epsilon = 0.00567222 \pm 0.00175868$   
 $\log_{10}\epsilon = -2.24625 \pm 0.134654$   
Fidelity 99.4328%

Fri 12 Jun 2015 15:11:42

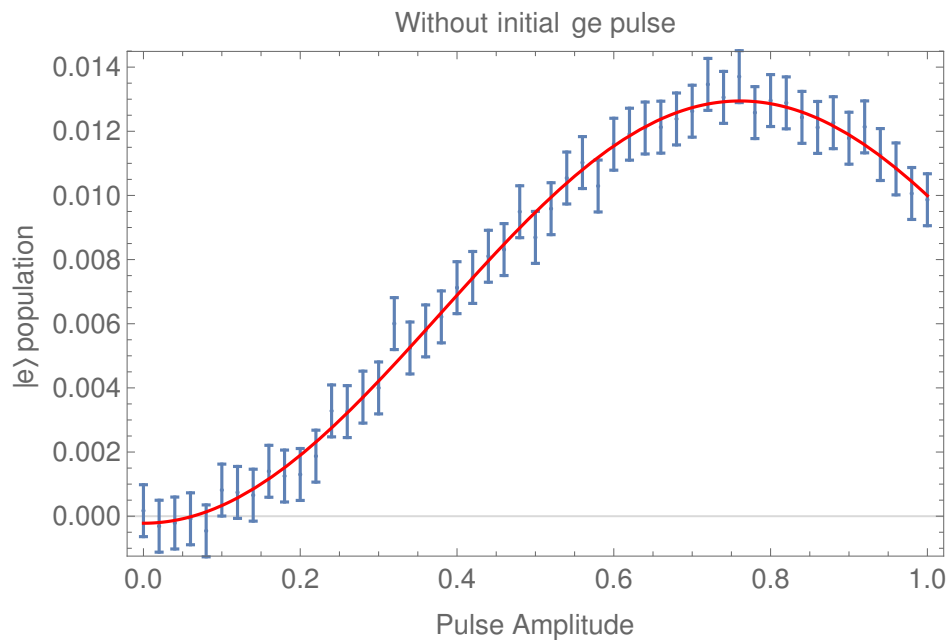
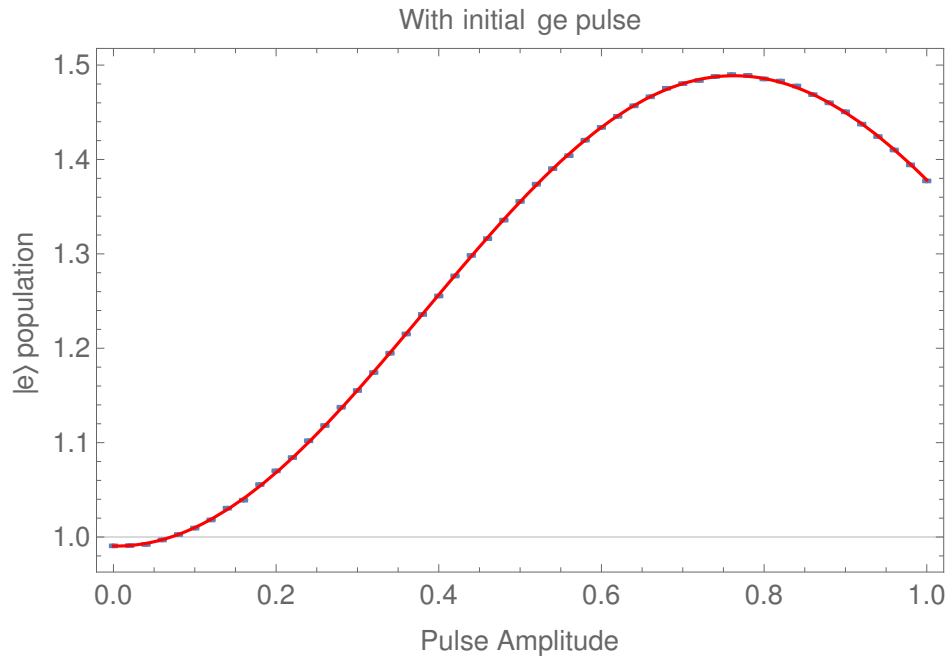
### 1088\_CZGate\_T1EF\_Qb4



$T_1$  EF [ $\mu\text{s}$ ] =  $3.20236 \pm 0.114981$   
 $\Delta T_1$  EF [ $\mu\text{s}$ ] = 0.403051  
 $T_1$  GE [ $\mu\text{s}$ ] = 4.78947

Wed 27 May 2015 09:04:58

## 1502\_RBPauliGate\_ThermalPop\_Qb2



$T_{\text{eff}} = 64.7203 \text{ mK}$   
 $p_e = 0.0265609$   
 $p_f = 0.000888119$



## Declaration of originality

The signed declaration of originality is a component of every semester paper, Bachelor's thesis, Master's thesis and any other degree paper undertaken during the course of studies, including the respective electronic versions.

Lecturers may also require a declaration of originality for other written papers compiled for their courses.

---

I hereby confirm that I am the sole author of the written work here enclosed and that I have compiled it in my own words. Parts excepted are corrections of form and content by the supervisor.

**Title of work** (in block letters):

Automatic Single Qubit Routines

**Authored by** (in block letters):

*For papers written by groups the names of all authors are required.*

**Name(s):**

Ciorciaro

**First name(s):**

Livio

With my signature I confirm that

- I have committed none of the forms of plagiarism described in the '[Citation etiquette](#)' information sheet.
- I have documented all methods, data and processes truthfully.
- I have not manipulated any data.
- I have mentioned all persons who were significant facilitators of the work.

I am aware that the work may be screened electronically for plagiarism.

**Place, date**

Zürich, 22.6.2015

**Signature(s)**

L. Ciorciaro

*For papers written by groups the names of all authors are required. Their signatures collectively guarantee the entire content of the written paper.*